Dynamic Modeling and Self-Tuning Anti-sway Control of a Seven Degree of Freedom Shipboard Knuckle Boom Crane

Iain A. Martin[a,*], Rishad A. Irani[a]

[a]Multi-Domain Laboratory, Department of Mechanical and Aerospace Engineering, Carleton University, Ottawa, Ontario, K1S 5B6, Canada

ARTICLE INFO

Abstract

A common type of crane found aboard many ships, knuckle boom cranes are complex, underactuated dynamic systems, and anti-sway control of such cranes is an important research problem for both operational efficiency and safety. This paper addresses the deficiency of research in anti-sway control for high degree of freedom (DOF) shipboard cranes by developing a dynamic model and anti-sway control system for a seven-DOF shipboard knuckle boom crane, mounted aboard a vessel that experiences six-DOF ship motion. The dynamic model is intended to provide fidelity beyond what is typically seen in literature, including the mass and inertia of the hydraulic actuators, sheaves and winch, along with internal actuator dynamics and a realistic cable fall angle.

The crane's kinematics are derived using both the standard transformation matrix approach and with dual quaternions, with the latter proving to be more computationally efficient for real-time deployment. Using the kinematics, the equations of motion of the seven-DOF knuckle boom crane are obtained with the Lagrange approach. To provide anti-sway control, a self-tuning anti-sway trajectory modifier is combined with a nonlinear sliding mode controller, built using the equations of motion of the crane. A nonlinear trajectory optimizer is used to track the desired, time-varying trajectory with the slew motor, winch motor, and the boom, jib and extension actuators. Tested in simulation on a ship with six-DOF motion at sea state 6, the system with self-tuning disabled provided a 64% reduction in the average root-mean-square-error (RMSE) between the desired and actual payload positions across the x and y trajectories. Allowing the anti-sway trajectory modifier to self-tune provided a 74% reduction in RMSE under the same conditions. When a sudden 5 kN disturbance force was applied to the payload in both the x and y axes, the system without the self-tuning showed a 58% reduction in the average RMSE across the x and y trajectories, while with self-tuning enabled showed a 77% reduction in RMSE. The self-tuning anti-sway control system was also shown to be robust to parameter uncertainties, where with parameter errors in the simulated crane ranging between $\pm 20\%$, the maximum increase in average RMSE found was only 6.3%; with self-tuning disabled, the maximum increase in average RMSE was 56%.

Within simulation, the anti-sway control system is shown to be highly effective at tracking a time-varying payload trajectory for a seven-DOF knuckle boom crane and reducing undesired payload motion, and is shown to be robust to both sudden disturbances and parameter uncertainties.

1. Introduction

Shipboard cranes play an important role in many maritime operations, and given the potential for operation at high sea states it is important to develop a control system that can maintain the position of the payload despite ship motion. However, cranes are underactuated systems and have more degrees of freedom (DOF) than can be controlled. For a shipboard knuckle boom crane, such as the one shown in Figure 1, the base, boom, jib and extension are fully actuated by the slew motor and hydraulic actuators, however the payload is free to swing and its exact position cannot by directly controlled in three dimensional space. Therefore, anti-sway control for cranes is an important and challenging control problem that has attracted the interest of researchers over the past several decades.

For a comprehensive review of general anti-sway control strategies, see Ramli et al. [24], who in recent years have been leaders in the field of input-shaping approaches to anti-sway crane control [23, 25]. A review of anti-sway control systems specific to shipboard cranes was published in 2020 by Cao and Li [5], who concluded that further work is needed to consider system disturbances, robustness to uncertainties and a more practical examination with

---

*Corresponding author

✉ IainMartin@cmail.carleton.ca (I.A. Martin); Rishad.Irani@carleton.ca (R.A. Irani)

ORCID(s): 0000-0001-6961-5861 (I.A. Martin); 0000-0003-2854-001X (R.A. Irani)

time-varying trajectories. Cao and Li also conclude that most existing research focuses on control of simplified two-DOF or three-DOF dynamic models for planar, two-dimensional cases, and that limited work has been performed for 3-dimensional cases with higher DOF cranes.

Some researchers who have considered anti-sway control for higher-DOF cranes include Kim and Park [14], who in 2017 considered a linearized model of a five-DOF container crane. In 2018, both Wang et al. [28] and Tysse and Egeland [26] developed control systems for a simplified model of a shipboard knuckle boom crane, without including the mass and inertia of the hydraulic actuators. In 2019 and 2020, Kim and Hong [16] and Kim [15] considered a four-DOF offshore container crane, developing both an adaptive sliding mode controller and a continuous sliding mode controller. Also in 2019, Maghsoudi et al. [17] considered a five-DOF gantry crane, a developed a neural-network based input shaper to provide sway reduction.

To address the sparse research in anti-sway control for time-varying trajectories and higher-DOF crane systems, Martin and Irani [18] considered a five-DOF shipboard gantry crane, perturbed by six-DOF ship motion to compare several anti-sway control strategies, and furthered their work by considering a six-DOF shipboard knuckle boom crane [19] (*pre-print*), with a dynamic model that included the mass and inertia of the hydraulic actuators, as well as internal actuator dynamics. An anti-sway control system was developed for both cranes that required both a generalized trajectory modifier, designed to provide anti-sway compensation, along with a suitable controller to allow the crane to track the modified trajectory [19]. To develop a suitable controller, it was found that while the industry-standard proportional-integral-derivative (PID) controller proved sufficient for the five-DOF gantry crane it was unable to adequately control the six-DOF knuckle boom crane. The knuckle boom crane required a nonlinear sliding-mode controller (SMC) [19]. The SMC is a powerful controller that can address the system robustness required for shipboard cranes, however to implement a sliding-mode controller on a shipboard knuckle boom crane a dynamic model of the crane is required.

Dynamic modeling of knuckle boom cranes has received some attention from researchers in the past decade. In a pair of papers published in 2013, Bak and Hansen [2, 3] developed a dynamic model and control system for a hydraulic knuckle boom crane used in pipe handling. Focusing on the electro-hydraulic control system, the crane considered by Bak and Hansen was planar with four degrees of freedom, and did not incorporate any anti-sway control. In 2018, Tysse and Egeland [26] modeled a six-DOF shipboard knuckle boom crane using screw theory and investigated the interaction between ship motion and pendulum sway, and in 2019 [27] developed an anti-sway controller using a Lyapunov-based pendulum damping and nonlinear MPC control system. In a series of papers between 2018 and 2020, Cibicik and Egeland [6, 8, 7] extended the screw theory, six-DOF knuckle boom crane model to include the mass and inertia of the hydraulic actuators, and investigated both the reaction forces experienced at the base of the crane during operation, as well as the effect of flexible links. In 2019, Wójcik et al. [1] developed a dynamic model for a six-DOF knuckle boom crane using the Lagrange approach that includes the masses and inertias of the actuators, but did not examine anti-sway control.

Given existing research has been limited to six-DOF knuckle boom cranes, this paper presents a dynamic model for a general seven-DOF shipboard knuckle boom crane with an extendable jib, a common feature on many cranes [12, 13, 22]. The dynamic model is intended to have higher fidelity than typically seen in the literature, and includes the mass and inertia of the hydraulic actuator cylinders and rods, the mass and inertia of the sheaves and winch, a realistic cable fall angle and internal actuator dynamics. The actuator responses are estimated with first-order transfer functions, and include deadzones with saturation limits. The equations of motion are derived using the Lagrange approach, and the kinematics of the crane developed using both transformation matrices and dual quaternions to compare computational efficiency. By providing a comprehensive dynamic model, developed in the current work, future researchers will be able to examine more shipboard crane operations and controller developments.

Additionally in the current work, anti-sway control is implemented on the simulated seven-DOF knuckle boom crane using a robust, generalized trajectory modification strategy with novel self-tuning parameters. The crane system is controlled with a SMC which utilize the crane's equations of motion. Furthermore, a new nonlinear trajectory optimizer is proposed to allow the overactuated crane tip to track the desired, time-varying trajectory.

The work herein addresses some of shortfalls and the suggested future research directions of Cao and Li [5]; specifically, higher degree of freedom systems, physical characteristics of shipboard cranes, time-varying trajectories, and system robustness. Thus, our paper contributes to the body of knowledge by providing a

1. sophisticated kinematic model of a seven-DOF knuckle boom crane in both a dual quaternion and transformation matrix form,

---

2. comprehensive method to dynamically determine the cable length on the crane and the appropriate cable-fall from the final sheave to the payload,

3. nonlinear trajectory optimizer which allows the crane to track time-varying trajectories, and

4. a self-tuning trajectory modification strategy for robust anti-sway control.

These contributions address many of the knowledge deficiencies or future research directions in the anti-sway control of shipboard cranes identified by Cao and Li [5].

The paper is organized such that Section 2 provides an overview of the seven-DOF knuckle boom crane considered in this work, and presents the coordinate frames assigned to each link using the Denavit-Hartenberg (DH) convention. Section 3 presents the dynamic model of the crane, where the kinematics are derived using both transformation matrices and dual quaternions. In Section 4 anti-sway control is implemented using the trajectory modifier, nonlinear trajectory optimizer and an SMC. Additionally, the simulation parameters and configurations is highlighted. Section 5 presents the results of four operational scenarios where disturbances and uncertainties are considered through the course of several case studies. The paper concludes with a summary of the results in Section 6.

2. The Seven-DOF Knuckle Boom Crane

Figure 1 shows a rendering of the seven-DOF knuckle boom crane which is the focus of the current work. The crane is modeled as fourteen rigid bodies connected by revolute and prismatic joints. The base of the crane has a mass m_0 and is free to rotate with respect to the ship deck coordinate frame $(XYZ)_D$ (or ground for a land-based crane), driven by a slew motor with inertia J_a that provides a torque τ_a. The boom has a mass m_1 and is articulated by the boom actuator, which has a cylinder mass m_{b1} and a rod mass m_{b2} and provides a force F_b. Likewise the jib has a mass m_2 and is articulated by the jib actuator, which has a cylinder mass m_{c1} and a rod mass m_{c2} and produces a force F_c. The jib can extend, actuated by a force F_d, and the jib extension has a mass m_3. The cylinder mass of the extension actuator is included in m_2, and the mass of the extension actuator rod included in m_3. The payload has a mass m_p, and the mass of all the cables is ignored. Attached to the boom is a winch with mass m_w, which provides a torque τ_w to raise and lower the payload via the cable. Also attached to the boom is the boom sheave (sheave 0), which has a mass m_{s0}. The jib sheave (sheave 1) has a mass m_{s1} and is attached to the jib, and the final sheave (sheave 2) has a mass m_{s2} and is attached to the end of the jib extension.

Figure 2 shows the seven degrees of freedom of the knuckle boom crane: the base rotates an angle θ_0, actuated by the slew motor; the boom actuator rod translates a distance d_1, actuated by the force F_b, and the jib actuator rod translates a distance d_2, actuated by the force F_c; the jib extension translates a distance d_3, actuated by the force F_d, and the cable length is adjusted by the winch, which rotates an angle of θ_w actuated by the torque τ_w; the payload hangs below the final sheave on a rigid cable with sway angles θ_6 and θ_7. Therefore, the degrees of freedom θ_0, d_1, d_2, d_3 and θ_w are directly actuated, while the sway angles θ_6 and θ_7 are unactuated. Figure 3 shows the dimensions required to parameterize the knuckle boom crane and used to develop the dynamic model. Note that the x, y and z subscripts are introduced in Figure 3 and are consistent with the assigned coordinate frames.

2.1. Coordinate Frame Assignment

To derive the kinematics of the knuckle boom crane coordinate frames must be assigned following the right-hand rule and are shown in Figures 4, 5 and 6. Using the Denavit-Hartenberg (DH) convention, a transformation from frame i to frame j can be described by four parameters,

- *Link Length a_i* - The distance along the X_j axis between the Z_i and the Z_j axes.

- *Link Twist α_i* - The rotation about the X_j axis required to align the Z_i axis with the Z_j axis.

- *Joint Distance d_i* - The distance along the Z_i axis between the X_i and X_j axes.

- *Joint Angle θ_i* - The rotation about the Z_i axis required to align the X_i axis with the X_j axis.

As the DH convention requires coordinate frames to be assigned along links in series, the kinematics of the knuckle boom crane is divided into three serial chains: the main kinematic chain, mapping the deck coordinate frame to the payload through the main components of the crane; the boom actuator kinematic chain, mapping the deck coordinate frame to the boom actuator rod; and the jib actuator kinematic chain, mapping the deck coordinate frame to the jib
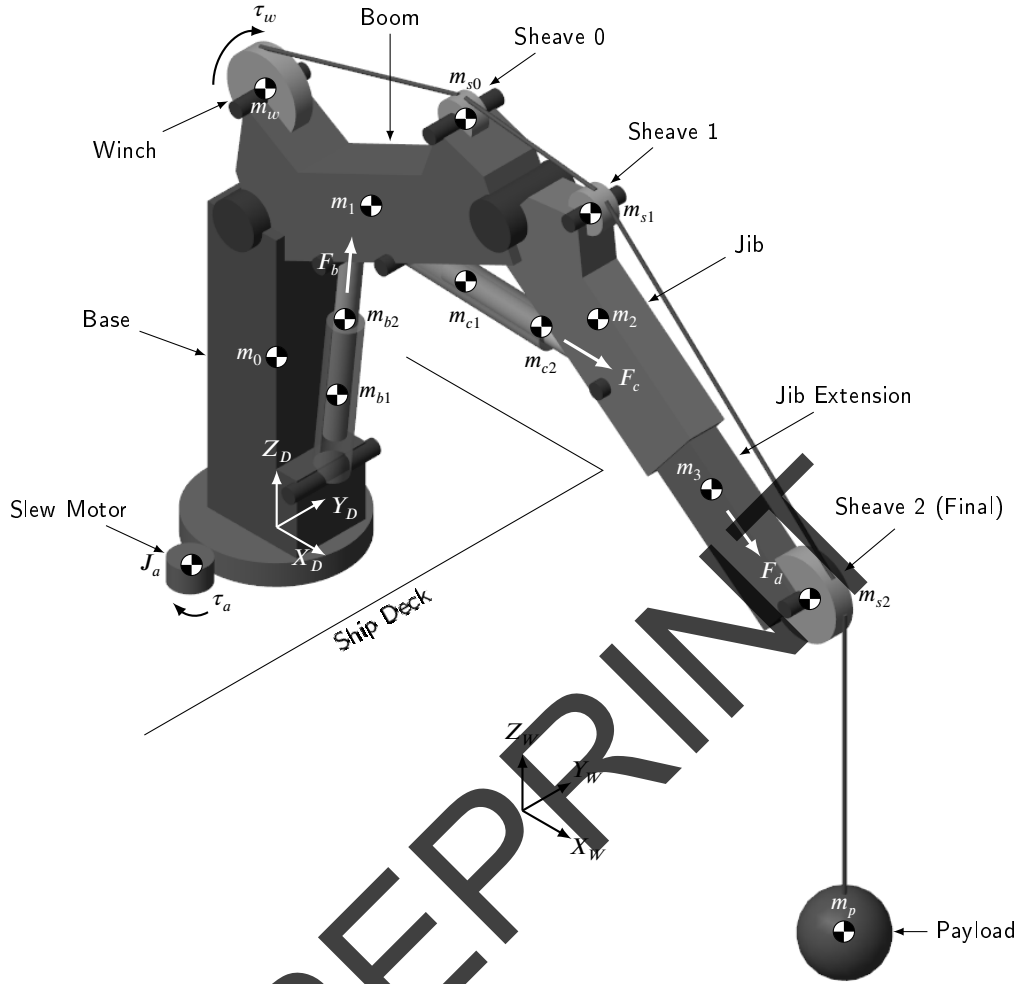
Figure 1: A 3D render of the knuckle boom crane with the locations of each centre of gravity, the applied forces, the deck coordinate frame $(XYZ)_D$ and the world (or ocean) coordinate frame $(XYZ)_W$.

actuator rod. A separate kinematic chain for the jib extension actuator is not required as the extension is included in the main kinematic chain.

Note that in Figures 4, 5 and 6 some angles are denoted with a negative sign, as the positive sense of each angle should be directed along the Z axis of the corresponding coordinate frame using the right-hand rule.

2.2. Main Kinematic Chain

Figure 4 shows the coordinate frames assigned to the main kinematic chain, where the origin coordinate frame is the deck coordinate frame $(XYZ)_D$, and Table 1 summarizes the associated DH parameters. The coordinate frame $(XYZ)_1$ can be reached by a rotation of θ_0 about the Z_D axis, a translation of l_0 along the Z_D axis followed by a rotation of $-90°$ about the X_1 axis. The coordinate frame $(XYZ)_2$ can be reached from the $(XYZ)_1$ frame by a rotation of θ_1 about the Z_1 axis, followed by a translation of l_1 along the X_2 axis. The tip of the jib $(XYZ)_3$ can then be reached by a rotation of θ_2 about the Z_2 axis, followed by a translation of l_2 along the X_3 axis.

The tip of the jib extension $(XYZ)_4$ can then be reached by a translation of d_3 along the X_4 axis, where d_3 is the displacement of the extension actuator. Thus, the extension actuator is included in the main kinematic chain. Considering Figure 4b, a rotation of $-90°$ about the Z_4 axis followed by a translation of l_4 along the X_5 axis aligns with coordinate frame $(XYZ)_5$. Coordinate frame $(XYZ)_6$, located at the tip of the final sheave can be reached follow a rotation of θ_5 about the Z_5 axis an a translation of r_2 along the X_6 axis.

In Figures 4b and 4c, the tip of the final sheave is modeled as a universal joint. The coordinate frame $(XYZ)_7$ is
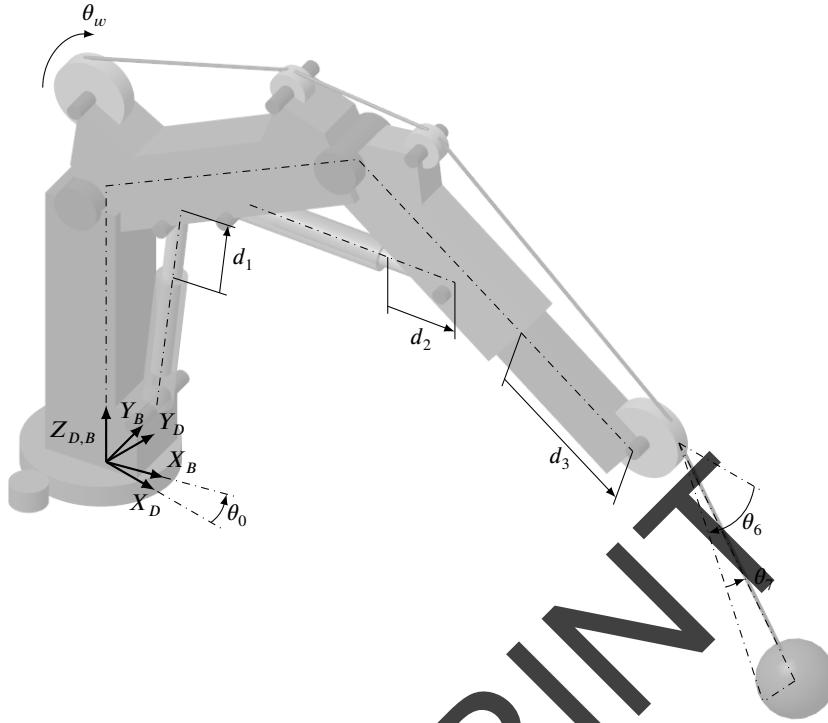
Figure 2: The seven degrees of freedom of the knuckle boom crane are the rotation angle of the base θ_0, the actuator extensions d_1 and d_2, the jib extension d_3, the cable reel out θ_w and the sway angles θ_6 and θ_7.

Table 1
DH Table - Main Kinematic Chain

Frame Transform	$\mathbf{a_i}$	α_i	$\mathbf{d_i}$	θ_i
$D \to 1$	0	$-90°$	l_0	θ_0
$1 \to 2$	l_1	0	0	θ_1
$2 \to 3$	l_2	0	0	θ_2
$3 \to 4$	d_3	0	0	0
$4 \to 5$	l_4	0	0	$-90°$
$5 \to 6$	r_2	0	0	θ_5
$6 \to 7$	0	$90°$	0	θ_6
$7 \to 8$	0	0	0	θ_7
$8 \to 9$	l_8	0	0	0

defined as a rotation of θ_6 about the Z_6 axis, followed by a rotation of $90°$ about the X_7 axis. The coordinate frame $(XYZ)_8$ is then defined as a rotation of θ_7 about the Z_7 axis. Finally, the payload coordinate frame $(XYZ)_9$ is reached following a translation of l_8 along the X_9 axis. To articulate the main kinematic chain, separate kinematic chains for the boom and jib actuators.

2.3. Boom Actuator Kinematic Chain

Figure 5 shows the coordinate frames assigned to the boom actuator kinematic chain, and Table 2 summarizes the DH parameters. The coordinate frame $(XYZ)_{b1}$ is reached following the rotation of θ_0 about the Z_D axis, then a rotation of $-90°$ about the X_{b1} axis. $(XYZ)_{b2}$ can then be reached following a rotation of θ_{b1} about the Z_{b1} axis and
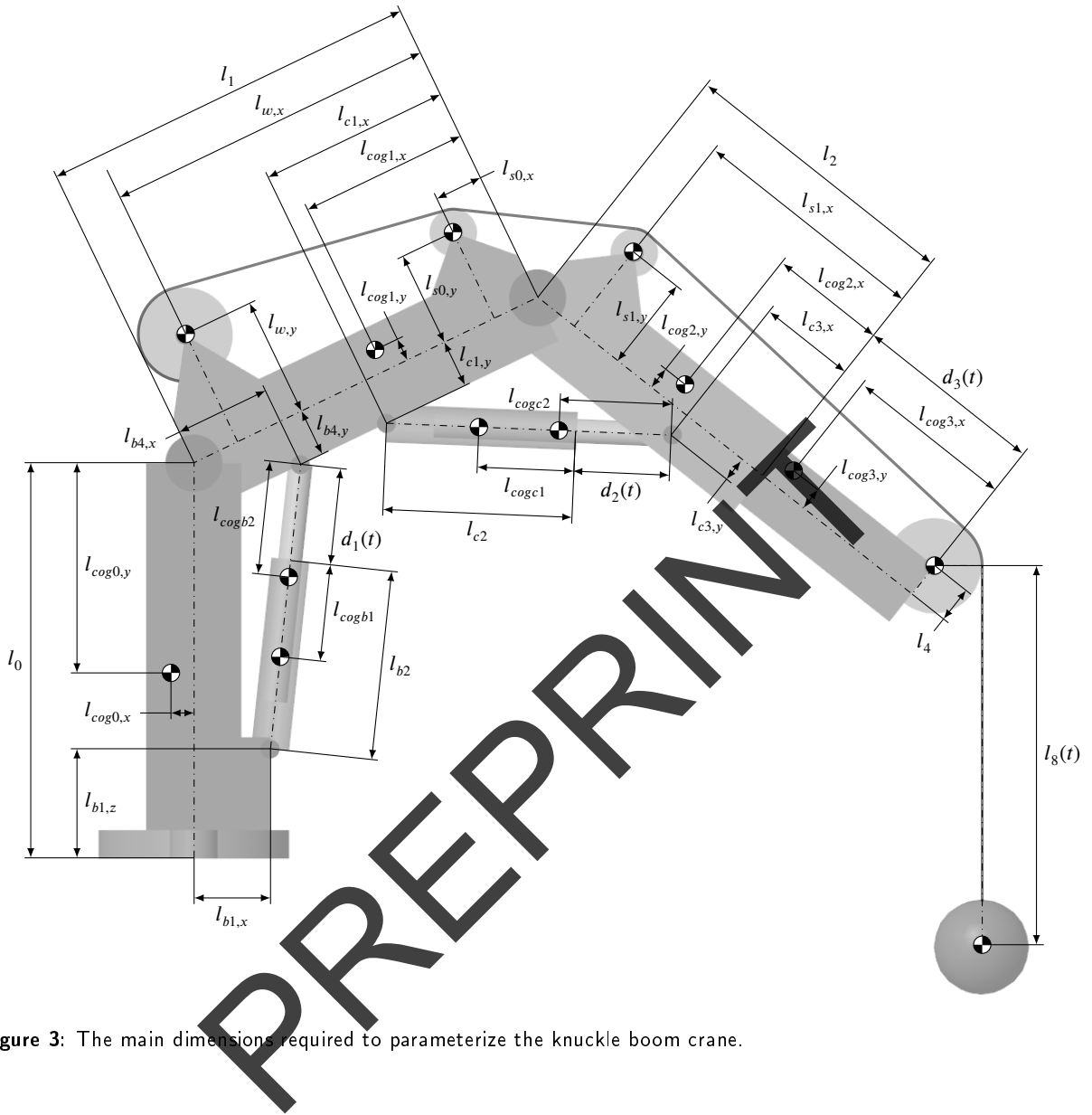
Figure 3: The main dimensions required to parameterize the knuckle boom crane.

a translation of l_{b1} along the X_{b2} axis, where

$$l_{b1} = \sqrt{(l_{b1,x})^2 + (l_{b1,z})^2}.$$ (1)

The coordinate frame $(XYZ)_{b3}$ can then be reached following a rotation of θ_{b2} about the Z_{b2} axis and a translation of l_{b2} along the X_{b3} axis. Finally, coordinate frame $(XYZ)_{b4}$ can be reached by a translation of d_1 along the X_{b4} axis.

2.4. Jib Actuator Kinematic Chain

Figure 6 shows the coordinate frames assigned to the jib actuator kinematic chain, and Table 3 summarizes the DH parameters. Starting at $(XYZ)_1$, coordinate frame $(XYZ)_{c1}$ can be reached following a rotation of θ_{c1} about the Z_1 axis and a translation of l_{c1} along the X_{c1} axis, where

$$l_{c1} = \sqrt{(l_1 - l_{c1,x})^2 + (l_{c1,y})^2}.$$ (2)
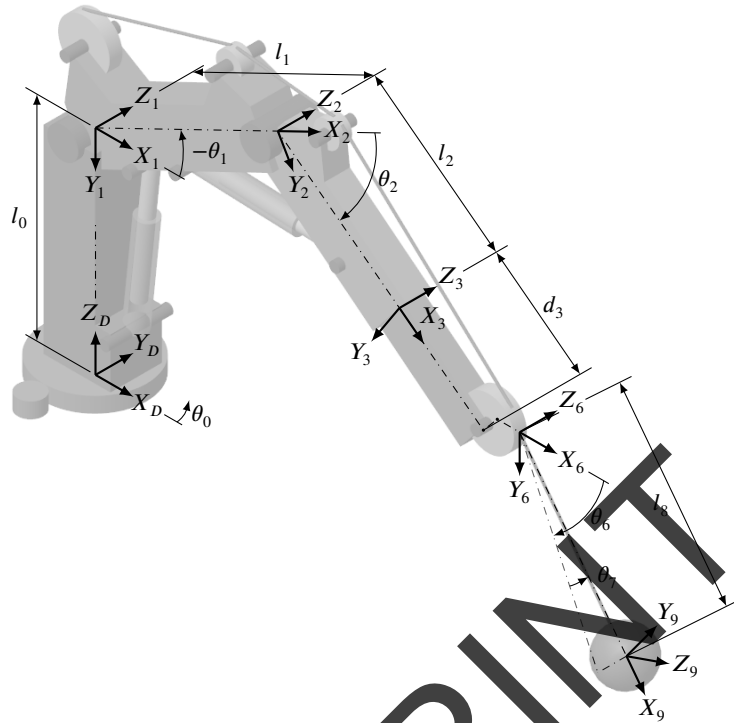
(a) The coordinate frames for the main kinematic chain.

(b) A view of the final sheave in the $(XZ)_B$ plane.

(c) A view of the final sheave in the $(YZ)_B$ plane.

Figure 4: The coordinate frames assigned to the main kinematic chain of the knuckle boom crane. Note that some angles are denoted with a negative sign, as the positive sense of each angle should be directed along the axis of the corresponding coordinate frame using the right-hand rule.

The coordinate frame $(XYZ)_{c2}$ can then be reached following a rotation of θ_{c2} about the Z_{c1} axis and a translation of l_{c2} along the X_{c2} axis. Finally, $(XYZ)_{c3}$ can be reached by a translation of d_2 along the X_{c3} axis. Table 3 provides the corresponding DH parameters for the jib actuator kinematic chain.

The coordinate frames assigned to the main chain, boom actuator chain and jib actuator chain are required to derive the kinematics of the knuckle boom crane, which will be needed to derive the equations of motion of the crane and implement the sliding mode controller.
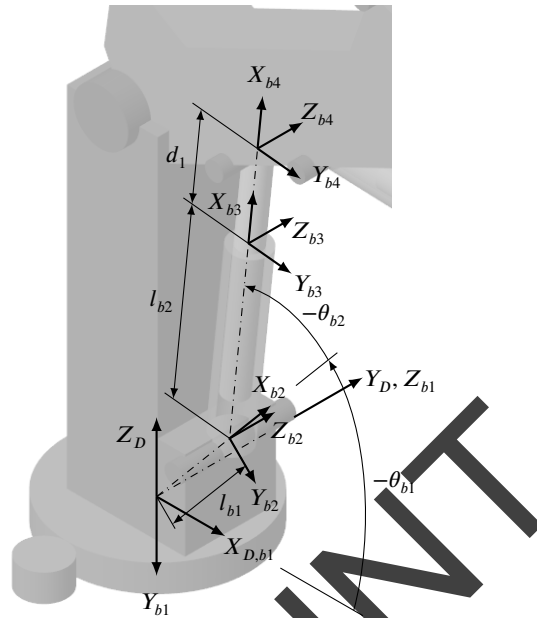
Figure 5: The coordinate frames for the boom actuator kinematic chain of the knuckle boom crane. Note that some angles are denoted with a negative sign, as the positive sense of each angle should be directed along the axis of the corresponding coordinate frame using the right-hand rule.

Table 2
DH Table - Boom Actuator Kinematic Chain

Frame Transform	$\mathbf{a_i}$	α_i	$\mathbf{d_i}$	θ_i
$D \to b1$	0	$-90°$	0	θ_0
$b1 \to b2$	l_{b1}	0	0	θ_{b1}
$b2 \to b3$	l_{b2}	0	0	θ_{b2}
$b3 \to b4$	d_1	0	0	0

Table 3
DH Table - Jib Actuator Kinematic Chain

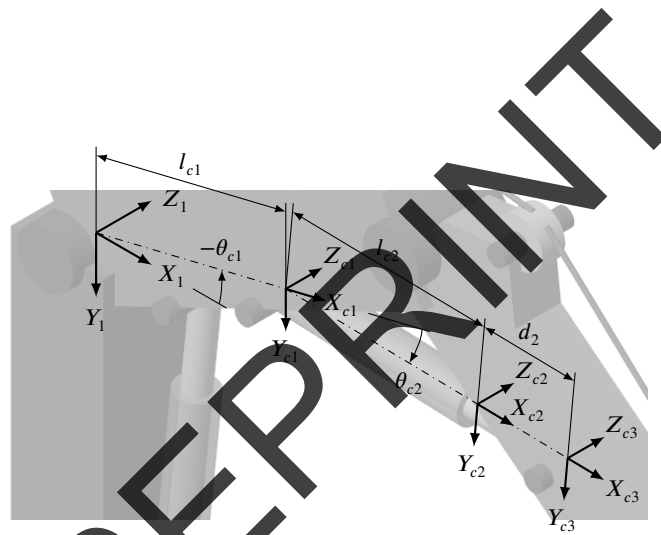| Frame Transform	$\mathbf{a_i}$	α_i	$\mathbf{d_i}$	θ_i
$1 \to c1$	l_{c1}	0	0	θ_{c1}
$c1 \to c2$	l_{c2}	0	0	θ_{c2}
$c2 \to c3$	d_2	0	0	0

Figure 6: The coordinate frames for the jib actuator kinematic chain of the knuckle boom crane. Note that some angles are denoted with a negative sign, as the positive sense of each angle should be directed along the axis of the corresponding coordinate frame using the right-hand rule.

3. Dynamic Modeling

Implementation of model based control such as a sliding mode controller requires the equations of motion of the crane, which in turn require kinematic expressions for each rigid body. In Section 3.1 the kinematics of the crane will be derived using transformation matrices, and in Section 3.2 the kinematics will be derived with dual quaternions. Sections 3.3 and 3.4 detail the correction for the gravity vector and the cable fall angle, respectively, and Section 3.5 presents the derivation of the equations of motion using the Lagrange approach.

3.1. Kinematics with Transformation Matrices

A transformation matrix ${}^{i}T_{j}$ provides a mapping between coordinate frames i and j using a 3×3 rotation matrix ${}^{i}R_{j}$ and 3×1 translation vector ${}^{i}\vec{p}_{j}$, combined into a 4×4 matrix

$$
{}^{i}T_{j} = \begin{bmatrix} & {}^{i}R_{j} & & {}^{i}\vec{p}_{j} \\ 0 & 0 & 0 & 1 \end{bmatrix}. \tag{3}
$$

Consider the four DH parameters presented in Section 2.1; a_i is a translation along the X_j axis, α_i a rotation about the X_j axis, d_i a translation along the Z_i axis and θ_i a rotation about the Z_i axis. Therefore, using the standard x and z rotation matrices the transformation from frame i to frame j expressed in DH parameters is

$$
{}^{i}T_{j} = \begin{bmatrix} \cos(\theta_i) & -\sin(\theta_i) & 0 & 0 \\ \sin(\theta_i) & \cos(\theta_i) & 0 & 0 \\ 0 & 0 & 1 & 0 \\ 0 & 0 & 0 & 1 \end{bmatrix} \begin{bmatrix} 1 & 0 & 0 & 0 \\ 0 & 1 & 0 & 0 \\ 0 & 0 & 1 & d_i \\ 0 & 0 & 0 & 1 \end{bmatrix} \begin{bmatrix} 1 & 0 & 0 & 0 \\ 0 & \cos(\alpha_i) & -\sin(\alpha_i) & 0 \\ 0 & \sin(\alpha_i) & \cos(\alpha_i) & 0 \\ 0 & 0 & 0 & 1 \end{bmatrix} \begin{bmatrix} 1 & 0 & 0 & 0 \\ 0 & 1 & 0 & 0 \\ 0 & 0 & 1 & a_i \\ 0 & 0 & 0 & 1 \end{bmatrix},
$$

$$
{}^{i}T_{j} = \begin{bmatrix} \cos(\theta_i) & -\sin(\theta_i)\cos(\alpha_i) & \sin(\theta_i)\sin(\alpha_i) & a_i\cos(\theta_i) \\ \sin(\theta_i) & \cos(\theta_i)\cos(\alpha_i) & -\cos(\theta_i)\sin(\alpha_i) & a_i\sin(\theta_i) \\ 0 & \sin(\alpha_i) & \cos(\alpha_i) & d_i \\ 0 & 0 & 0 & 1 \end{bmatrix}, \tag{4}
$$

providing a general mapping of the four DH parameters to the corresponding transformation matrix ${}^{i}T_{j}$. Using the DH parameters presented in Tables 1, 2 and 3, transformation matrices ${}^{D}T_{i}$ were defined relating each centre of mass i back to the deck coordinate frame and are given in Appendix A. Note that the DH parameters are defined in terms of intermediate joint angles θ_1, θ_2, θ_{b1}, θ_{b2}, θ_{c1} and θ_{c2}, and expressions relating each intermediate angle to the actuator extensions d_1 and d_2 are provided in Appendix B.

As the Lagrange approach will be used to derive the equations of motion of the seven-DOF knuckle boom crane, the velocities of each centre of mass i are required. Given that the last column of ${}^{D}T_{i}$ contains the relative position vector ${}^{D}\vec{p}_{i}$, the last column of the time derivative of the transformation matrix will provide the 3×1 relative velocity vector ${}^{D}\dot{\vec{p}}_{i}$,

$$
\begin{Bmatrix} {}^{D}\dot{\vec{p}}_{i} \\ 1 \end{Bmatrix} = {}^{D}\dot{T}_{i} \begin{Bmatrix} 0 \\ 0 \\ 0 \\ 1 \end{Bmatrix}, \tag{5}
$$

where ($\dot{}$) denotes a derivative with respect to time. To obtain the angular velocities of each centre of mass, the velocity transformation matrix ${}^{D}V_{i}$ can be found by multiplying the time derivative of the transformation matrix by the inverse of the transformation matrix,

$$
{}^{D}V_{i} = {}^{D}\dot{T}_{i} \, {}^{D}T_{i}^{-1} = \begin{bmatrix} & {}^{D}\omega_{i} & & {}^{D}v_{i} \\ 0 & 0 & 0 & 1 \end{bmatrix}, \tag{6}
$$

where $^D\omega_i$ is the 3×3 angular velocity tensor,

$$^D\omega_i = \begin{bmatrix} 0 & -^D(\omega_z)_i & ^D(\omega_y)_i \\ ^D(\omega_z)_i & 0 & -^D(\omega_x)_i \\ -^D(\omega_y)_i & ^D(\omega_x)_i & 0 \end{bmatrix} \tag{7}$$

Therefore, the 3×1 angular velocity vector $^D\vec{\omega}_i$ containing the angular velocities of centre of mass i with respect to the deck coordinate frame can be built as $^D\vec{\omega}_i = \begin{bmatrix} ^D(\omega_x)_i & ^D(\omega_y)_i & ^D(\omega_z)_i \end{bmatrix}^T$.

The winch will also have an angular velocity $\dot{\theta}_w$ directed in the Z_w axis, given by

$$\dot{\theta}_w = \frac{l_8 + l_c}{r_w} \tag{8}$$

where l_8 is the length of cable from the tip of the sheave to the payload, and l_c is the total length of cable running from the tip of the sheave back to the winch, calculated using the crane geometry in Appendix C. Therefore, $\dot{\theta}_w$ must be mapped to the deck coordinate frame and added to $^D\vec{\omega}_w$. The angular velocity tensor Ω_w corresponding to $\dot{\theta}_w$ is given by,

$$\Omega_w = \begin{bmatrix} 0 & -\dot{\theta}_w & 0 \\ \dot{\theta}_w & 0 & 0 \\ 0 & 0 & 0 \end{bmatrix}. \tag{9}$$

Mapping Ω_w to the deck coordinate frame using the rotation matrix $^D R_w$,

$$^D\Omega_w = {}^D R_w \cdot \Omega_w \cdot {}^D R_w^T = \begin{bmatrix} 0 & -^D(\Omega_z)_w & ^D(\Omega_y)_w \\ ^D(\Omega_z)_w & 0 & -^D(\Omega_x)_w \\ -^D(\Omega_y)_w & ^D(\Omega_x)_w & 0 \end{bmatrix}. \tag{10}$$

Therefore, the angular velocity vector $^D\vec{\omega}_w$ for the winch can be written as,

$$^D\vec{\omega}_w = \begin{Bmatrix} ^D(\omega_x)_w + ^D(\Omega_x)_w \\ ^D(\omega_y)_w + ^D(\Omega_y)_w \\ ^D(\omega_z)_w + ^D(\Omega_z)_w \end{Bmatrix}. \tag{11}$$

A similar procedure is employed for the sheaves, where the angular velocity tensor for each sheave can be written in terms of the winch angular velocity $\dot{\theta}_w$,

$$\Omega_{s0} = \begin{bmatrix} 0 & -\dot{\theta}_w\left(\frac{r_w}{r_0}\right) & 0 \\ \dot{\theta}_w\left(\frac{r_w}{r_0}\right) & 0 & 0 \\ 0 & 0 & 0 \end{bmatrix}, \quad \Omega_{s1} = \begin{bmatrix} 0 & -\dot{\theta}_w\left(\frac{r_w}{r_1}\right) & 0 \\ \dot{\theta}_w\left(\frac{r_w}{r_1}\right) & 0 & 0 \\ 0 & 0 & 0 \end{bmatrix}, \quad \Omega_{s2} = \begin{bmatrix} 0 & -\dot{\theta}_w\left(\frac{r_w}{r_2}\right) & 0 \\ \dot{\theta}_w\left(\frac{r_w}{r_2}\right) & 0 & 0 \\ 0 & 0 & 0 \end{bmatrix}. \tag{12}$$

While the use of transformation matrices is a standard in the robotics community, another arguably more efficient method of deriving the kinematics of multi-body robots [10] are dual-quaternions.

3.2. Kinematics with Dual Quaternions

Quaternions were first proposed by Hamilton [11] as a way of representing the pose of an object using three parameters to define the orientation of a line in space, and a fourth to represent a rotation about that line. Dual-quaternions are hypercomplex extensions of quaternions introduced by Clifford [9] that contain information about both the orientation of a rigid body as well as its displacement.

A quaternion q can be written as a 4-tuple (q_0, q_1, q_2, q_3), where q_0 is a scalar and the elements q_1, q_2 and q_3 form a 3×1 vector $\vec{q} = q_1\hat{i} + q_2\hat{j} + q_3\hat{k}$. Translation information can be included by adding a dual component $\epsilon\left(p_0 + \vec{p}\right)$ to

the quaternion to create a dual quaternion Q,

$$Q = q_0 + \vec{q} + \epsilon \left(p_0 + \vec{p} \right). \tag{13}$$

The vector $\vec{p}$ is defined as $\vec{p} = p_1 \hat{i} + p_2 \hat{j} + p_3 \hat{k}$, and ϵ is defined such that $\epsilon^2 = 0$. The dual quaternion Q is then an 8-tuple given by $Q = (q_0, q_1, q_2, q_3, p_0, p_1, p_2, p_3)$.

Transformations between rigid bodies can be described using concatenations of dual quaternions. To multiply two dual quaternions, the dual quaternion product is used,

$$Q_a \otimes Q_b = q_{(0,ab)} + \vec{q}_{(ab)} + \epsilon \left(p_{(0,ab)} + \vec{p}_{(ab)} \right), \tag{14}$$

where,

$$q_{(0,ab)} = q_{(0,a)} q_{(0,b)} - \vec{q}_a \left(\vec{q}_b \right)^T, \tag{15}$$

$$\vec{q}_{(ab)} = q_{(0,a)} \vec{q}_b + q_{(0,b)} \vec{q}_a + \vec{q}_a \times \vec{q}_b, \tag{16}$$

$$p_{(0,ab)} = p_{(0,a)} q_{(0,b)} - \vec{p}_a \left(\vec{q}_b \right)^T + q_{(0,a)} p_{(0,b)} - \vec{q}_a \left(\vec{p}_b \right)^T, \tag{17}$$

$$\vec{p}_{(ab)} = q_{(0,a)} \vec{p}_b + p_{(0,b)} \vec{q}_a + \vec{q}_a \times \vec{p}_b + p_{(0,a)} \vec{q}_b + q_{(0,b)} \vec{p}_a + \vec{p}_a \times \vec{q}_b. \tag{18}$$

Once coordinate frames have been assigned and the DH parameters determined, the corresponding dual quaternions can be generated in a straight-forward manner. The link length a_i is a translation along the X_j axis, the link twist α_i a rotation about the X_j axis, the joint distance d_i a translation along the Z_i axis and θ_i a rotation about the Z_i axis. Therefore, a transformation from frame i to frame j can be built from 4 dual quaternions, each corresponding to one of the four DH parameters a, α, d and θ,

$$^iQ_{j,a} = 1 + \begin{bmatrix} 0 & 0 & 0 \end{bmatrix} + \epsilon \left(0 + \begin{bmatrix} a_i & 0 & 0 \end{bmatrix} \right), \tag{19}$$

$$^iQ_{j,\alpha} = \cos\left(\frac{\alpha_i}{2}\right) + \begin{bmatrix} \sin\left(\frac{\alpha_i}{2}\right) & 0 & 0 \end{bmatrix} + \epsilon \left(0 + \begin{bmatrix} 0 & 0 & 0 \end{bmatrix} \right), \tag{20}$$

$$^iQ_{j,d} = 1 + \begin{bmatrix} 0 & 0 & 0 \end{bmatrix} + \epsilon \left(0 + \begin{bmatrix} 0 & 0 & d_i \end{bmatrix} \right), \tag{21}$$

$$^iQ_{j,\theta} = \cos\left(\frac{\theta_i}{2}\right) + \begin{bmatrix} 0 & 0 & \sin\left(\frac{\theta_i}{2}\right) \end{bmatrix} + \epsilon \left(0 + \begin{bmatrix} 0 & 0 & 0 \end{bmatrix} \right), \tag{22}$$

Therefore, the complete dual quaternion representing the transformation from frame i to j expressed in terms of the DH parameters is,

$$^iQ_j = {}^iQ_{j,\theta} \otimes {}^iQ_{j,d} \otimes {}^iQ_{j,\alpha} \otimes {}^iQ_{j,a}, \tag{23}$$

$$= q_{0,ij} + \vec{q}_{ij} + \epsilon \left(p_{0,ij} + \vec{p}_{ij} \right), \tag{24}$$

where,

$$q_{0,ij} = \cos\left(\frac{\theta_i}{2}\right) \cos\left(\frac{\alpha_i}{2}\right), \tag{25}$$

$$\vec{q}_{ij} = \left\{ \begin{matrix} \cos\left(\frac{\theta_i}{2}\right) \sin\left(\frac{\alpha_i}{2}\right) \\ \sin\left(\frac{\theta_i}{2}\right) \sin\left(\frac{\alpha_i}{2}\right) \\ \sin\left(\frac{\theta_i}{2}\right) \cos\left(\frac{\alpha_i}{2}\right) \end{matrix} \right\}^T, \tag{26}$$

$$p_{0,ij} = -d_i \sin\left(\frac{\theta_i}{2}\right) \cos\left(\frac{\alpha_i}{2}\right) - a_i \cos\left(\frac{\theta_i}{2}\right) \sin\left(\frac{\alpha_i}{2}\right), \tag{27}$$

$$\vec{p}_{ij} = \left\{ \begin{array}{c} a_i \cos\left(\frac{\theta_i}{2}\right) \cos\left(\frac{\alpha_i}{2}\right) - d_i \sin\left(\frac{\theta_i}{2}\right) \cos\left(\frac{\alpha_i}{2}\right) \\ a_i \sin\left(\frac{\theta_i}{2}\right) \cos\left(\frac{\alpha_i}{2}\right) + d_i \cos\left(\frac{\theta_i}{2}\right) \sin\left(\frac{\alpha_i}{2}\right) \\ -a_i \sin\left(\frac{\theta_i}{2}\right) \sin\left(\frac{\alpha_i}{2}\right) + d_i \cos\left(\frac{\theta_i}{2}\right) \cos\left(\frac{\alpha_i}{2}\right) \end{array} \right\}^T . \tag{28}$$

Equations (24)-(28) are therefore analogous to equation (4), expressing the transformation from frame i to frame j as a function of the four DH parameters. Using the DH parameters presented in Tables 1, 2 and 3, dual quaternions $^D Q_i$ were defined relating each centre of mass i back to the deck coordinate frame, and are given in Appendix D. Each dual quaternion contains information about both the rotation and translation of the centre of mass with respect to the deck. To extract only the translational component, the product between the dual quaternion $^D Q_i$ and the inverse rotation quaternion $\left(^D Q_{i,r}\right)^{-1}$ where,

$$^D Q_i = q_{0,i} + \vec{q}_i + \epsilon(p_{0,i} + \vec{p}_i), \tag{29}$$

$$\left(^D Q_{i,r}\right)^{-1} = q_{0,i} - \vec{q}_i + \epsilon\left(0 + \begin{bmatrix} 0 & 0 & 0 \end{bmatrix}\right), \tag{30}$$

thus, dual quaternion product between $^D Q_i$ and $\left(^D Q_{i,r}\right)^{-1}$ gives

$$^D Q_i \otimes \left(^D Q_{i,r}\right)^{-1} = 1 + \begin{bmatrix} 0 & 0 & 0 \end{bmatrix} + \epsilon\left(^D p_i + ^D \vec{p}_i\right), \tag{31}$$

where $^D \vec{p}_i$ contains the deck frame position of centre of mass i as an $\begin{bmatrix} \hat{i} & \hat{j} & \hat{k} \end{bmatrix}$ vector in the deck coordinate frame. The velocity of each centre of mass $^D \vec{p}_i$ can be then found simply by taking a derivative of $^D \vec{p}_i$ with respect to time,

$$^D \dot{\vec{p}}_i = \frac{d\left(^D \vec{p}_i\right)}{dt}. \tag{32}$$

To calculate the angular velocity of each centre of mass, derivatives can be taken of the rotational components of the dual quaternion. Given the dual quaternion $^D Q_i = q_{0,i} + \vec{q}_i + \epsilon(p_{0,i} + \vec{p}_i)$, the required derivatives are,

$$\dot{q}_{0,i} = 2\frac{d\left(q_{0,i}\right)}{dt}, \tag{33}$$

$$\dot{\vec{q}}_i = 2\frac{d\left(\vec{q}_i\right)}{dt}, \tag{34}$$

The angular velocity vector $^D \vec{\omega}_i$ can then be found by multiplying through the inverse of the rotation quaternion,

$$^D \vec{\omega}_i = \dot{q}_{0,i}(-\vec{q}_i) + q_{0,i}\dot{\vec{q}}_i + \dot{\vec{q}}_i \times (-\vec{q}_i) \tag{35}$$

Note as was the case when deriving the kinematics with the transformation matrices, the winch and sheaves each have their own angular velocity related to the velocity of the cable. The winch angular velocity tensor Ω_w, equation 9, was rotated into the deck coordinate frame using equation 10, giving an angular velocity vector $^D \vec{\omega}_w$ as,

$$^D \vec{\omega}_w = \dot{q}_{0,w}(-\vec{q}_w) + q_{0,w}\dot{\vec{q}}_w + \dot{\vec{q}}_w \times (-\vec{q}_w) + \begin{bmatrix} ^D(\Omega_x)_w & ^D(\Omega_y)_w & ^D(\Omega_z)_w \end{bmatrix} \tag{36}$$

where $^D Q_w = q_{0,w} + \vec{q}_w + \epsilon(p_{0,w} + \vec{p}_w)$. The same procedure, equations (29)-(36) must also be applied to the sheaves to obtain $\Omega_{s0,s1,s2}$ in the dual quaternion form. Since the kinematics of the crane have been derived with respect to the deck coordinate frame rather than the world coordinate frame, the gravity vector for the deck coordinate frame must be determined.

3.3. Gravity Vector Correction

As the mass and inertia of the ship are not considered in the equation of motion derivation, it is therefore convenient to derive the dynamics of the knuckle boom crane treating the deck coordinate frame as the origin frame. However,

---

since the gravity vector is aligned with the Z_W axis rather than the Z_D axis, the gravity vector must be rotated into the $(XYZ)_D$ frame. The ship rotates about the world frame by three angles; using the *Yaw-Pitch-Roll* rotation sequence, the first rotation can be taken about Z_W axis by a yaw angle Ψ_y, with a positive sense defined as a rotation of the bow to port. The second rotation can be taken about the $X_{W'}$ axis by a pitch angle Φ_p, with a positive sense defined as the bow tipping down. The third rotation can be taken about the $Y_{W''}$ axis by a roll angle Θ_r, with a positive sense defined as the port side up. The three consecutive rotation matrices can then be defined as

$$
{}^{W'}R_W = \begin{bmatrix} \cos(\Psi_y) & \sin(\Psi_y) & 0 \\ \sin(\Psi_y) & \cos(\Psi_y) & 0 \\ 0 & 0 & 1 \end{bmatrix}, \tag{37}
$$

$$
{}^{W''}R_{W'} = \begin{bmatrix} 1 & 0 & 0 \\ 0 & \cos(\Phi_p) & -\sin(\Phi_p) \\ 0 & \sin(\Phi_p) & \cos(\Phi_p) \end{bmatrix}, \tag{38}
$$

$$
{}^{W'''}R_{W''} = \begin{bmatrix} \cos(-\Theta_r) & 0 & \sin(-\Theta_r) \\ 0 & 1 & 0 \\ -\sin(-\Theta_r) & 0 & \cos(-\Theta_r) \end{bmatrix}, \tag{39}
$$

where the angle Θ_r is negated as the positive sense of the rotation is defined according to marine standards and is reversed compared to traditional robotic and aerospace convention.

Therefore a point in the deck coordinate frame $\vec{p}_D = \begin{bmatrix} p_{x,D} & p_{y,D} & p_{z,D} \end{bmatrix}^T$ can be mapped to a point in the world coordinate frame $\vec{P}_W = \begin{bmatrix} P_{x,W} & P_{y,W} & P_{z,W} \end{bmatrix}^T$ by,

$$
\vec{P}_W = \begin{bmatrix} {}^{W'}R_W \end{bmatrix} \begin{bmatrix} {}^{W''}R_{W'} \end{bmatrix} \begin{bmatrix} {}^{W'''}R_{W''} \end{bmatrix} \vec{p}_D \tag{40}
$$

Note that the multiplication sequence is important when concatenating rotation matrices; mapping vector $\vec{p}_D$ to vector $\vec{P}_W$ using equation (40) involves first a rotation of $\vec{p}_D$ using ${}^{W'''}R_{W''}$, then a rotation using ${}^{W''}R_{W'}$, and finally a rotation using ${}^{W'}R_W$. Therefore, the reverse mapping is

$$
\vec{p}_D = \begin{bmatrix} {}^{W'''}R_{W''} \end{bmatrix}^{-1} \begin{bmatrix} {}^{W''}R_{W'} \end{bmatrix}^{-1} \begin{bmatrix} {}^{W'}R_W \end{bmatrix}^{-1} \vec{P}_W \tag{41}
$$

As it is desired to map the world frame gravity vector $\vec{g}_W = \begin{bmatrix} 0 & 0 & g \end{bmatrix}^T$ to a vector $\vec{g}_D$ in the deck coordinate frame, the sequence given in equation (41) should be used. Note that the inverse of any rotation matrix is simply it's transpose, giving,

$$
\begin{aligned}
\vec{g}_D &= \begin{bmatrix} {}^{W'''}R_{W''} \end{bmatrix}^T \begin{bmatrix} {}^{W''}R_{W'} \end{bmatrix}^T \begin{bmatrix} {}^{W'}R_W \end{bmatrix}^T \vec{g}_W, \\
&= \left\{ \begin{array}{c} \sin(\Theta_r)\cos(\Phi_p)g \\ \sin(\Phi_p)g \\ \cos(\Theta_r)\cos(\Phi_p)g \end{array} \right\}.
\end{aligned} \tag{42}
$$

Along with the corrected gravity vector, a more accurate cable fall angle θ_5 must be developed.

3.4. Cable Fall Angle

Typically, a cable fall is modeled as a universal joint at a fixed location on the final sheave [1, 7, 28]. However, with both the ship and crane in six-DOF motion relative to the world frame, the cable fall location on the final sheave is dynamic and not simply a fixed point. Thus, to improve the dynamic model beyond the current literature, a more accurate cable fall angle is developed.

The payload hangs below the final sheave by a rigid cable of length l_8, attached to a universal joint located at coordinate frame $(XYZ)_6$. Given the natural tendency of the cable and payload to align with the gravity vector, the fall angle θ_5 will change due to both the current crane position and the ship's orientation to ensure the X_6 axis lies
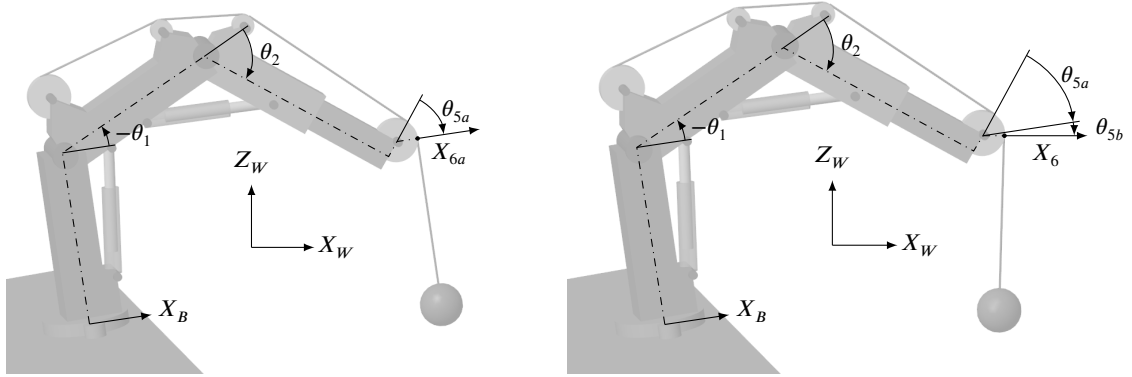
(a) The fall angle when X_6 is aligned with X_B.

(b) The fall angle when X_6 is in plane with $(XY)_W$.

Figure 7: The cable fall angle should take into account both the crane's position and the ship's orientation.

parallel to the $(XY)_W$ plane.

Figure 7a shows the case where θ_5 only considers the current crane position, θ_{5a} is set such that the X_{6a} axis is always parallel with the X_B axis,

$$\theta_{5a} = \frac{\pi}{2} - \theta_1 - \theta_2. \tag{43}$$

A more realistic situation is shown in Figure 7b where the X_6 axis is instead parallel to the plane $(XY)_W$. Therefore, the true fall angle should consider the ship's orientation in addition to the current crane orientation. The additional component θ_{5b} can be found by first rotating X_6 into the world frame, achieved using the rotation matrix sequence defined given in equation (40),

$$^W R_D = \left[{}^{W'} R_W \right] \left[{}^{W''} R_{W'} \right] \left[{}^{W'''} R_{W''} \right], \tag{44}$$

which maps a rotation from the deck coordinate frame back to the world frame. Note that X_6 is defined in the same plane as X_B, and therefore must also be rotated back through the angle θ_0 about the Z_D axis,

$$^D R_B = \begin{bmatrix} \cos(\theta_0) & -\sin(\theta_0) & 0 \\ \sin(\theta_0) & \cos(\theta_0) & 0 \\ 0 & 0 & 1 \end{bmatrix}. \tag{45}$$

Therefore, expressing the $X_6 = \begin{bmatrix} 1 & 0 & 0 \end{bmatrix}^T$ vector in the world coordinate frame can be accomplished by first rotating X_6 to the deck frame, followed by a rotation to the world frame,

$$
\begin{aligned}
{}^6 X_W &= {}^W R_D {}^D R_B \begin{Bmatrix} 1 \\ 0 \\ 0 \end{Bmatrix}, \\
&= \begin{Bmatrix} \left[c(\Theta_r)c(\Psi_y) + s(\Theta_r)s(\Phi_p)s(\Psi_y) \right] c(\theta_0) - c(\Phi_p)s(\Psi_y)s(\theta_0) \\ \left[c(\Theta_r)s(\Psi_y) - s(\Theta_r)s(\Phi_p)c(\Psi_y) \right] c(\theta_0) + c(\Phi_p)c(\Psi_y)s(\theta_0) \\ s(\Theta_r)c(\Phi_p)c(\theta_0) + s(\Phi_p)s(\theta_0) \end{Bmatrix},
\end{aligned} \tag{46}
$$

where $\cos()$ and $\sin()$ are abbreviated $c()$ and $s()$, respectively. The angle θ_{5b} can then be found by taking a dot product

between the ^6X_W and the vector $Z_W = \begin{bmatrix} 0 & 0 & 1 \end{bmatrix}^T$,

$$\theta_{5b} = \frac{\pi}{2} - \cos^{-1}\left(^6X_W \bullet Z_W\right), \tag{47}$$

$$= \frac{\pi}{2} - \cos^{-1}\left[\sin(\Theta_r)\cos(\Phi_p)\cos(\theta_0) + \sin(\Phi_p)\sin(\theta_0)\right] \tag{48}$$

Therefore, the fall angle θ_5 is given by

$$\theta_5 = \theta_{5a} + \theta_{5b} \tag{49}$$

With the kinematics derived and consideration made for the gravity vector, cable routing and fall angle, the dynamic equations of motion can be formulated.

3.5. Equations of Motion

With the complete kinematics of the seven-DOF knuckle boom crane derived using both transformation matrices and dual quaternions, the equations of motion can be obtained to allow control of the crane using an SMC. Using the Lagrange approach, the crane is modeled with 14 centres of mass, so the Lagrangian L is given by,

$$L = \sum_{i=0}^{14} K_i - \sum_{i=0}^{14} U_i, \tag{50}$$

where for rigid body i, K_i and U_i are the kinetic and potential energies, respectively. The kinetic energy for each body can be written as

$$K_i = \frac{1}{2}m_i\left(^D\vec{p}_i \bullet {}^D\vec{p}_i\right) + \frac{1}{2}{}^D\vec{\omega}_i^T \cdot {}^DI_i \cdot {}^D\vec{\omega}_i, \tag{51}$$

where m_i is the mass of rigid body i and ^DI_i is the inertia matrix of rigid body i transformed into the deck coordinate frame,

$$^DI_i = {}^DR_i \cdot I_i \cdot (^DR_i)^T. \tag{52}$$

Note that the kinetic energy of the slew motor K_a is given as

$$K_a = \frac{1}{2}J_a\left(N\dot{\theta}_0\right)^2, \tag{53}$$

where N is the gear ratio between the angular velocity of the slew motor ω_{slew} and the angular velocity of the ring gear ω_{ring} attached to the base of the crane, $N = \omega_{slew}/\omega_{ring}$.

The potential energy U_i of rigid body i can be written as

$$U_i = m_i \cdot (\vec{g}_D)^T \cdot {}^D\vec{p}_i. \tag{54}$$

The equations of motion of the knuckle boom crane can then be derived using the Lagrange equation,

$$\frac{d}{dt}\left(\frac{\partial L}{\partial \dot{\mathbf{q}}}\right) - \frac{\partial L}{\partial \mathbf{q}} = \mathbf{F}, \tag{55}$$

where $\mathbf{q} = \begin{bmatrix} \theta_0 & d_1 & d_2 & d_3 & \theta_w & \theta_6 & \theta_7 \end{bmatrix}^T$ are the seven degrees of freedom of the knuckle boom crane, and $\mathbf{F} = \begin{bmatrix} -N\tau_a & F_b & F_c & F_d & \tau_w & 0 & 0 \end{bmatrix}^T$ is the 7×1 vector of applied forces. Taking the required derivatives, the equations of motion take the form

$$M\ddot{\mathbf{q}} + \mathbf{a} = \mathbf{F}, \tag{56}$$

where M is the 7×7 nonlinear mass matrix, and $\mathbf{a}$ is a 7×1 nonlinear vector.

As a control system for a real crane will operate on hardware and in real-time, it is desirable to keep the equations of motion of the crane as concise as possible to reduce the computation time of the sliding control law, which must calculate M, $\mathbf{a}$ and $\dot{\mathbf{a}}$ each time-step. To compare efficiency, expressions for M, $\mathbf{a}$ and $\dot{\mathbf{a}}$ were calculated with both the transformation matrix kinematics, presented in Section 3.1, and with the dual quaternions developed in Section 3.2. Both sets of equations were derived using Maple, and after utilizing the Maple *simplify* and *collect* commands and converting to MATLAB code, the dual quaternions provided code that was 30% shorter than with the transformation matrices. The complete equations of motion calculated with the dual quaternions are provided as a supplementary file, along with instructions for usage and deployment. As a contribution to the field, the derivations outlined in this section can assist future researchers and industrial practitioners to examine seven-DOF cranes. With the equations of motion now derived, a model-based control system for the anti-sway compensation of the knuckle boom crane can be implemented.

4. Control and Simulation

The control problem considered, is to maintain the payload at a desired position with respect to the ship deck. The operator provides a desired trajectory x_d, y_d and z_d for the crane tip, expressed in the deck coordinate frame $(XYZ)_D$, and a desired cable length l_d. For the knuckle boom crane model developed in this work, the tip coordinate frame is considered to be coincident with $(XYZ)_6$.

To provide a virtual crane simulator to act as a digital twin for a physical knuckle boom crane, the seven-DOF knuckle boom crane was built in MATLAB/Simulink using the Simscape Multibody toolbox, with the 3D render shown previously in Figure 1. The digital twin is actuated by the slew motor, winch motor, and hydraulic actuators, corresponding to forces/torques τ_a, τ_w, F_b, F_c and F_d in Figure 1. Note that while the equations of motion were built to accurately represent the digital twin, some elements are not included in the SMC and equations of motion, such as acutator deadzones and saturation limits. The system will also be tested in real-time with a fixed sampling frequency, and with parameter variations between the digital twin and the equations of motion used in the SMC. To facilitate the testing, the SMC and control algorithms were implemented on a National Instruments real-time controller which communicated via TCP with the MATLAB/Simulink digital twin. Feedback signals from the digital twin were returned to the real-time controller via the TCP link.

Figure 8 shows the overall structure of the control system. The desired trajectory vector $\mathbf{x}_d$ is first modified by a trajectory modifier, described in Section 4.1 to produce a modified trajectory vector $\mathbf{x}_{dm}$. The modified trajectory is then converted into an actuator setpoint vector $\mathbf{q}_d$ using a nonlinear trajectory optimizer, described in Section 4.2. The actuator setpoints and the current actuator states $\mathbf{q}$, obtained from the virtual Simscape crane, are then provided to the SMC described in Section 4.4, which uses the equations of motion of the crane to provide a control action vector $\mathbf{u}$. Actuator dynamics described in section 4.3 are then applied to convert the control actions $\mathbf{u}$ into force inputs $\mathbf{F}_a$ for the Simscape simulation. Each vector can be written as

$$\mathbf{x}_d = \begin{bmatrix} x_d & y_d & z_d & l_d & 0 & 0 \end{bmatrix}^T, \tag{57}$$

$$\mathbf{x}_{dm} = \begin{bmatrix} x_{dm} & y_{dm} & z_{dm} & l_{dm} & \theta_{6,dm} & \theta_{7,dm} \end{bmatrix}^T, \tag{58}$$

$$\mathbf{q}_d = \begin{bmatrix} \theta_{0,d} & d_{1,d} & d_{2,d} & d_{3,d} & \theta_{w,d} & \theta_{6,d} & \theta_{7,d} \end{bmatrix}^T, \tag{59}$$

$$\mathbf{u} = \begin{bmatrix} u_1 & u_2 & u_3 & u_4 & u_5 & 0 & 0 \end{bmatrix}^T, \tag{60}$$

$$\mathbf{F}_a = \begin{bmatrix} \tau_a & F_b & F_c & F_d & \tau_w & 0 & 0 \end{bmatrix}^T, \tag{61}$$

$$\mathbf{q} = \begin{bmatrix} \theta_0 & d_1 & d_2 & d_3 & \theta_w & \theta_6 & \theta_7 \end{bmatrix}^T. \tag{62}$$

The following subsections detail the operation of each component of the control system.

4.1. Self-Tuning Anti-Sway Trajectory Modification

As proposed in [19], anti-sway control can be introduced by modifying the desired trajectory before the control actions are calculated. Consider the case shown in Figure 9; if the tip of the crane, indicated by the small black circle is positioned at the point x_d, the payload will not reach the desired position, indicated by the dashed lines due to rolling motion of the ship. However, if the tip of the crane is positioned at the point x_{dm}, the natural tendency of the payload to align with the gravity vector will allow the payload to reach the desired position. The trajectory modification system
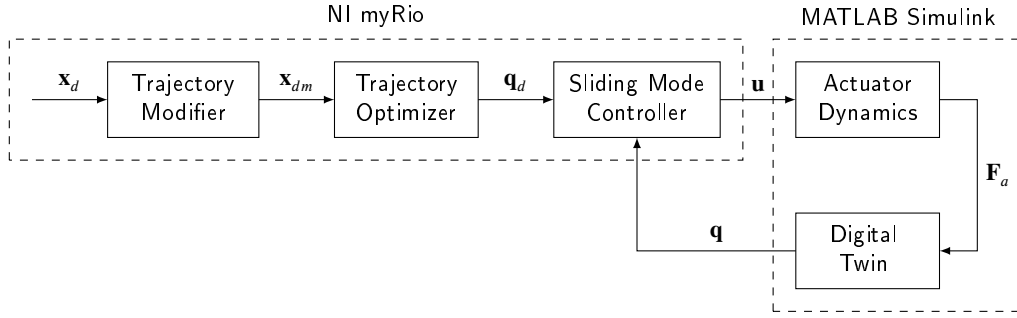
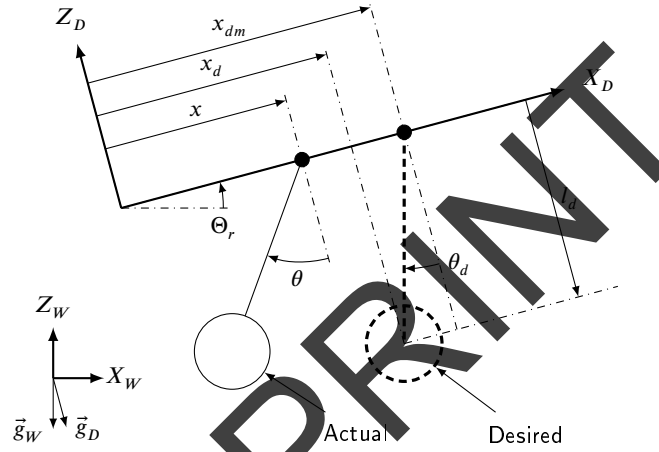Figure 8: The overall structure of the knuckle boom crane control system.

Figure 9: The trajectory modification strategy, where the small black circles represents the crane tip, coordinate frame $(XYZ)_6$ and the white circles represent the payload. The actual position of the tip and payload is represented by the thin, solid lines, and the desired position of the cart and payload represented by the thick, dashed lines.

used in [19] for a six-DOF knuckle boom crane, adapted to the notation of this paper is

$$x_{dm} = x_d + l_d \tan(\Theta_r), \tag{63}$$

$$y_{dm} = y_d + l_d \tan(\Phi_p), , \tag{64}$$

$$z_{dm} = z_d, \tag{65}$$

$$l_{dm} = \frac{l_d}{\cos(\Theta_r)\cos(\Phi_p)}, \tag{66}$$

$$\theta_{6,dm} = \Theta_r + \theta_{offset}, \tag{67}$$

$$\theta_{7,dm} = \Phi_p + \phi_{offset}, \tag{68}$$

where Θ_r and Φ_p are the ship's current roll and pitch angles, and θ_{offset} and ϕ_{offset} are only needed to ensure $\theta_{6,dm}$ and $\theta_{7,dm}$ are measured with respect to the Z_D axis. This trajectory modification system provided an 84% reduction in the payload tracking root-mean-square-error (RMSE) for the six-DOF knuckle boom crane used in [19].

For the present work, the same trajectory modification system was used. Given how the cable fall angle θ_5 has been modeled to align the X_6 axis with the $(XY)_W$ plane, the angle $\theta_{6,dm}$ should always equal $\pi/2$ to align with the gravity vector; therefore, the offset angles θ_{offset} and ϕ_{offset} can be written as

$$\theta_{offset} = \frac{\pi}{2} - \Theta_r, \tag{69}$$
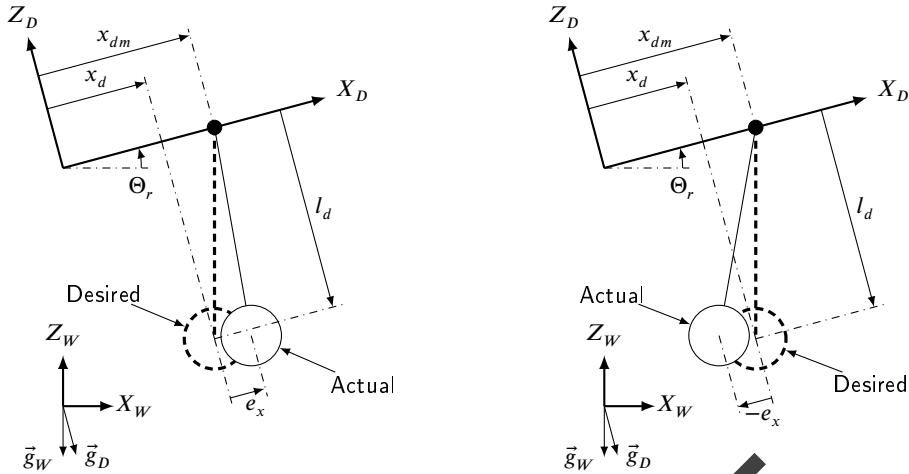
(a) The case where both the signs of $\tan(\Theta_r)$ and the position error e_x are the same. The desired payload position is represented by the thick dashed line, while the actual payload position is represented by the thin solid line.

(b) The case where the signs of $\tan(\Theta_r)$ and the position error e_x are not the same. The desired payload position is represented by the thick dashed line, while the actual payload position is represented by the thin solid line.

Figure 10: The cases considered when developing the self-tuning trajectory modifier.

$$\phi_{offset} = 0, \tag{70}$$

When applying the trajectory modification [19] to the seven-DOF knuckle boom crane, it was found in simulation trials that the x_{dm} and y_{dm} trajectories provided poor performance compared to the results obtained with the original six-DOF knuckle boom crane—which does not feature a jib extension. Note that a significant difference in operation between the six and seven-DOF knuckle boom cranes is in the calculation of the actuator setpoint vector $\mathbf{q}_d$ from the modified trajectory vector $\mathbf{x}_{dm}$; as the tip of the six-DOF crane is fully actuated, the actuator setpoints can be computed directly using the inverse kinematics [19]. However, for the seven-DOF knuckle boom crane the crane tip is overactuated, and the proposed nonlinear trajectory optimizer, detailed in Section 4.2 is required to determine the setpoints for the five actuators from the four desired trajectories x_{dm}, y_{dm}, z_{dm} and l_{dm}.

To improve the anti-sway performance of the system, self-tuning parameters ξ_x, ξ_y, ξ_z and ξ_l are introduced to equations (63)-(66), providing new trajectory modification equations,

$$x_{dm} = x_d + (1 + \xi_x)l_d \tan(\Theta_r), \tag{71}$$

$$y_{dm} = y_d + (1 + \xi_y)l_d \tan(\Phi_p), \tag{72}$$

$$z_{dm} = z_d + \xi_z, \tag{73}$$

$$l_{dm} = \frac{l_d}{\cos(\Theta_r)\cos(\Phi_p)} + \xi_l. \tag{74}$$

For the dimensionless scaling gains ξ_x and ξ_y, first consider the case shown in Figure 10a; if the payload is pulled too far along the X_D axis, then the error between the actual and desired payload positions will be a positive error e_x, matching the positive sign of $\tan(\Theta_r)$. The modified trajectory x_{dm} should therefore be reduced to align the payload with the desired position. Likewise, if the payload error e_x is negative, as in Figure 10b, then the trajectory x_{dm} should be increased to align the payload with the desired position. Upon initialization, $\xi_x = \xi_y = 0$ and equations 71-74 are equivalent to 63-66. With units of length, the self-tuning offsets ξ_z and ξ_l are added to reduce the effect of uncertain mass parameters; if the crane components or payload are heavier than predicted by the SMC, the desired trajectories z_d and l_d can be offset by a distance proportional to the error e_z and e_l between the actual and desired trajectories. The four self-tuning parameters can be calculated as

$$\xi_x = \xi_x' + \begin{cases} -\varrho_x & \text{if } \text{sgn}(e_x) = \text{sgn}(\tan(\Theta_r)) \text{ and } \xi_x > \xi_{x,min} \\ \varrho_x & \text{if } \text{sgn}(e_x) \neq \text{sgn}(\tan(\Theta_r)) \text{ and } \xi_x < \xi_{x,max} \\ 0 & \text{otherwise} \end{cases}, \tag{75}$$

$$\xi_y = \xi_y' + \begin{cases} -\varrho_y & \text{if } \text{sgn}(e_y) = \text{sgn}(\tan(\Phi_p)) \text{ and } \xi_y > \xi_{y,min} \\ \varrho_y & \text{if } \text{sgn}(e_y) \neq \text{sgn}(\tan(\Phi_p)) \text{ and } \xi_y < \xi_{y,max} \\ 0 & \text{otherwise} \end{cases}, \tag{76}$$

$$\xi_z = \xi_z' + \begin{cases} e_z \varrho_z & \text{if } \xi_{z,min} < \xi_z < \xi_{z,max} \\ 0 & \text{otherwise} \end{cases}, \tag{77}$$

$$\xi_l = \xi_l' + \begin{cases} e_l \varrho_l & \text{if } \xi_{l,min} < \xi_l < \xi_{l,max} \\ 0 & \text{otherwise} \end{cases}, \tag{78}$$

where the ($'$) designation indicates the gains from the previous timestep, and ϱ_x, ϱ_y, ϱ_z and ϱ_l are the growth rates. To ensure stability of the control system, bounds are added to each gain, $\xi_{x,min/max}$, $\xi_{y,min/max}$, $\xi_{z,min/max}$ and $\xi_{l,min/max}$ to limit the modified trajectories x_{dm}, y_{dm}, z_{dm} and l_{dm}. The bounds should be selected to ensure the tip trajectory does not grow too large; for the present work, the bounds were selected as $\xi_{x,min} = \xi_{y,min} = 0.5$, $\xi_{x,max} = \xi_{y,max} = 1.5$, $\xi_{z,min} = \xi_{l,min} = -1$ and $\xi_{z,min} = \xi_{l,min} = 1$. As noted in Figure 8, the output of the trajectory modifier must be converted to actuator setpoints using a nonlinear trajectory optimizer.

4.2. Nonlinear Trajectory Optimization

The desired position of the payload is expressed as a trajectory x_d, y_d and z_d along the X_D, Y_D and Z_D axes, along with a cable length l_d. Using the trajectory modification system for the crane tip given in equations (71)-(73), the desired position of the tip coordinate frame $(XYZ)_6$ with respect to the deck is given by x_{dm}, y_{dm} and z_{dm}. However, since the tip is actuated by four independent actuators providing forces/torques τ_a, F_b, F_c and F_d, the corresponding actuator setpoints to track the desired trajectory cannot be directly calculated using the inverse kinematics of the crane.

Instead, the trajectory can be generated using a nonlinear optimization function. In this work, an optimizer based on the Gauss-Newton method is used [4], which takes the form

$$\mathbf{x}_{i+1} = \mathbf{x}_i + \delta_i, \tag{79}$$

where

$$\delta_i = -\kappa \left[\nabla f(\mathbf{x}_i)\right]^{-1} f(\mathbf{x}_i), \tag{80}$$

and the vector $\mathbf{x} = \begin{bmatrix} \theta_{0,dm} & d_{1,dm} & d_{2,dm} & d_{3,dm} \end{bmatrix}^T$ contains the desired actuator setpoints to track the trajectory x_{dm}, y_{dm} and z_{dm}, and i corresponds to the current iteration of the optimization. The nonlinear system of equations $f(\mathbf{x})$ is to be minimized such that $f(\mathbf{x}) = 0$.

To generate the system of equations $f(\mathbf{x})$, the forward kinematics of the crane can be solved by taking the elements in the first three rows and last column of the transformation matrix $^DT_6$, giving the position of coordinate frame $(XYZ)_6$ with respect to the deck coordinate frame, $^Dx_6$, $^Dy_6$ and $^Dz_6$ as

$$^Dx_6 = f_1 = \Big[\big[(r_2 \sin(\theta_5) + d_3 + l_2)\cos(\theta_2) + (r_2 \cos(\theta_5) + l_4)\sin(\theta_2) + l_1\big]\cos(\theta_1)$$
$$+ \big[(r_2 \cos(\theta_5) + l_4)\cos(\theta_2) - (r_2 \sin(\theta_5) + d_3 + l_2)\sin(\theta_2)\big]\sin(\theta_1)\Big]\cos(\theta_0), \tag{81}$$

$$^Dy_6 = f_2 = \Big[\big[(r_2 \sin(\theta_5) + d_3 + l_2)\cos(\theta_2) + (r_2 \cos(\theta_5) + l_4)\sin(\theta_2) + l_1\big]\cos(\theta_1)$$
$$+ \big[(r_2 \cos(\theta_5) + l_4)\cos(\theta_2) - (r_2 \sin(\theta_5) + d_3 + l_2)\sin(\theta_2)\big]\sin(\theta_1)\Big]\sin(\theta_0), \tag{82}$$

$$^Dz_6 = f_3 = \big[(-r_2 \sin(\theta_5) - d_3 - l_2)\cos(\theta_2) + (-r_2 \cos(\theta_5) - l_4)\sin(\theta_2) - l_1\big]\sin(\theta_1)$$

$$+ \left[(r_2 \cos(\theta_5) + l_4) \cos(\theta_2) - \sin(\theta_2)(r_2 \sin(\theta_5) + d_3 + l_2) \right] \cos(\theta_1) + l_0 \tag{83}$$

Another condition to consider is the minimization of the change of each actuator setpoint between timesteps,

$$f_{4,i} = (\theta_{0,dm} - \theta'_{0,dm})^2 + (d_{1,dm} - d'_{1,dm})^2 + (d_{2,dm} - d'_{2,dm})^2 + (d_{3,dm} - d'_{3,dm})^2 \tag{84}$$

where the $(')$ designation refers to the optimized actuator setpoints from the previous timestep. By minimizing f_4 the optimizer reduces the likehood of sudden changes in the actuator setpoints. Therefore, the system $f(\mathbf{x})$ can be expressed as

$$f(\mathbf{x}) = \begin{cases} f_1 - x_{dm} = 0 \\ f_2 - y_{dm} = 0 \\ f_3 - z_{dm} = 0 \\ f_4 = 0 \end{cases} \tag{85}$$

Considering Equation (79), δ acts as a velocity, providing a 4×1 vector $\delta = \begin{bmatrix} \delta_1 & \delta_2 & \delta_3 & \delta_4 \end{bmatrix}^T$ that describes the change in actuator setpoint between each timestep. To avoid rapid changes in actuator setpoints, velocity limits $\delta_{max} = \begin{bmatrix} \delta_{1,max} & \delta_{2,max} & \delta_{3,max} & \delta_{4,max} \end{bmatrix}^T$ were introduced such that

$$\delta_j = \begin{cases} \delta_j & \text{if } |\delta_j| \le \delta_{j,max} \\ \text{sgn}(\delta_j) \cdot \delta_{j,max} & \text{otherwise} \end{cases} \tag{86}$$

where $j = 1, 2, 3, 4$. The optimization function can be run for a chosen number of iterations i_{max}, or until the norm of the errors $(f_1 - x_{dm})$, $(f_2 - y_{dm})$ and $(f_3 - z_{dm})$ is below a chosen threshold. In this work, the threshold was chosen to be 1 mm to avoid excessive computation. To avoid the oversimplification of direct action of the crane's components, actuator dynamics are considered within the digital twin.

4.3. Actuator Dynamics

To estimate hydraulic actuator dynamics, first-order transfer functions were applied to each actuator, taking the form

$$\frac{F_i(s)}{U_i(s)} = \frac{b_i}{s + b_i}, \tag{87}$$

where s is the Laplace variable and F_i the force or torque applied by actuator i on the crane, corresponding to $F_1 = \tau_a$, $F_2 = F_b$, $F_3 = F_c$, $F_4 = F_d$ and $F_5 = \tau_w$. $U_i(s)$ is the control effort supplied by the SMC, and $b_i > 0$ are constants; therefore, the performance of each actuator is governed by a first-order response with a time constant $\tau_i = 1/b_i$. Converting equation (87) to state space form,

$$\dot{\gamma} = -b\gamma + \mathbf{u}, \tag{88}$$
$$\mathbf{F}_a = b\gamma, \tag{89}$$

where γ is the state vector, $b = \text{diag}[b_1, b_2, b_3, b_4, b_5, b_6, b_7]$ a diagonal matrix, and $\mathbf{F}_a = \begin{bmatrix} F_1 & F_2 & F_3 & F_4 & F_5 & 0 & 0 \end{bmatrix}^T$ is the vector of applied forces.

Before the forces $\mathbf{F}_a$ are applied to the digital twin, deadzones of ± 100 N and ± 100 Nm are applied to each actuator, along with saturation limits of ± 50 kNm for both the slew motor and winch motor, ± 600 kN for the boom actuator, ± 200 kN for the jib actuator and ± 100 kN for the jib extension actuator.

4.4. Sliding Mode Control

As previously found [19], a PID controller was incapable of controlling a six-DOF knuckle boom crane due to the nonlinear dynamics. Thus, a stable sliding mode controller was developed for the six-DOF knuckle boom crane with a final control law

$$\mathbf{u} = \dot{\gamma} + b\gamma + b^{-1}\dot{\mathbf{u}}_1 + \mathbf{u}_2 \tag{90}$$

where,

$$\mathbf{u}_1 = -k_\alpha \mathrm{sat}\left(\Phi_\alpha \mathbf{s}_1\right), \tag{91}$$

$$\mathbf{u}_2 = -k_\beta \mathrm{sat}\left(\Phi_\beta \mathbf{s}_2\right), \tag{92}$$

$$\boldsymbol{\gamma} = b^{-1}\left(M\ddot{\mathbf{q}}_d - M\lambda\dot{\mathbf{e}} + \mathbf{a}\right). \tag{93}$$

Modifying the six-DOF SMC for the current seven-DOF crane, we can say that the matrices $k_\alpha = \mathrm{diag}[k_{\alpha,1}, k_{\alpha,2}, k_{\alpha,3}, k_{\alpha,4}, k_{\alpha,5}, k_{\alpha,6}, k_{\alpha,7}]$, $k_\beta = \mathrm{diag}[k_{\beta,1}, k_{\beta,2}, k_{\beta,3}, k_{\beta,4}, k_{\beta,5}, k_{\beta,6}, k_{\beta,7}]$, $\Phi_\alpha = \mathrm{diag}[\Phi_{\alpha,1}, \Phi_{\alpha,2}, \Phi_{\alpha,3}, \Phi_{\alpha,4}, \Phi_{\alpha,5}, \Phi_{\alpha,6}, \Phi_{\alpha,7}]$ and $\Phi_\beta = \mathrm{diag}[\Phi_{\beta,1}, \Phi_{\beta,2}, \Phi_{\beta,3}, \Phi_{\beta,4}, \Phi_{\beta,5}, \Phi_{\beta,6}, \Phi_{\beta,7}]$ are constant, diagonal gain matrices, with the vectors $\mathbf{s}_1$ and $\mathbf{s}_2$ given by,

$$\mathbf{s}_1 = \dot{\mathbf{e}} + \lambda\mathbf{e}, \tag{94}$$

$$\mathbf{s}_2 = -\mathbf{u}_1, \tag{95}$$

where $\lambda = \mathrm{diag}[\lambda_1, \lambda_2, \lambda_3, \lambda_4, \lambda_5, \lambda_6, \lambda_7]$ is a constant, diagonal gain matrix, and the error vector $\mathbf{e}$ is

$$\mathbf{e} = \begin{bmatrix} \theta_0 - \theta_{0,dm} \\ d_1 - d_{1,dm} \\ d_2 - d_{2,dm} \\ d_3 - d_{3,dm} \\ \theta_w - \theta_{w,dm} \\ \theta_6 - \theta_{6,dm} \\ \theta_7 - \theta_{7,dm} \end{bmatrix}. \tag{96}$$

A benefit of control with an SMC is robustness to uncertainties and parameter variations due to the addition of the control actions $\mathbf{u}_1$ and $\mathbf{u}_2$, an area of improvement identified by Cao and Li [5]. Additionally, Cao and Li [5] also identified time-varying trajectories as area of interest which can be examined through simulation.

4.5. Simulation and Time-Varying Trajectory

Within the current work, simulations were run at 100 Hz. The desired time-varying trajectories were selected as,

$$\dot{x}_d = \dot{y}_d = \begin{cases} 0.1 \text{ m/s} & t < 12 \text{ s} \\ 0 \text{ m/s} & t \geq 12 \text{ s} \end{cases}, \tag{97}$$

$$\dot{z}_d = \begin{cases} 0.2 \text{ m/s} & t < 12 \text{ s} \\ 0 \text{ m/s} & t \geq 12 \text{ s} \end{cases}, \tag{98}$$

$$\dot{l}_d = \begin{cases} 0 \text{ m/s} & t \leq 20 \text{ s} \\ 0.1 \text{ m/s} & 20 < t < 35 \text{ s} \\ 0 \text{ m/s} & t \geq 35 \text{ s} \end{cases}. \tag{99}$$

The ship motion used in the simulations corresponded to sea state 6, and was generated with ShipMo3D, a validated software package [20, 21]. Table 4 lists the RMS of the ship motion for each degree of freedom. The sea way was modeled with regular waves of the Bretschneider spectrum using a significant wave height of 5 metres and a period of 12.4 seconds. The ship used was the generic frigate included in ShipMo3D, sailing at a speed of 6.000 kt with a heading of 15.0° into the sea. The frequency of the ship's roll, pitch and yaw motion was 0.093 Hz.

The gains for the SMC and trajectory optimizer were tuned to reduce the RMSE error in the payload trajectory tracking and are provided in Appendix E, along with the inertial and geometric properties used in the simulation. The initial configuration of the crane was set to $\theta_0 = 0°$, $d_1 = 0.5$ m, $d_2 = 0.5$ m, $d_3 = 0$ m, and a cable length $l_8 = 4$ m, corresponding to a winch rotation $\theta_w = 25.2$ rad, or 12.6 m of total cable. To test the effectiveness of the proposed modelling and anti-sway system, several simulation studies were performed.

Table 4
Ship Motion Parameters

	Surge (m)	Sway (m)	Heave (m)	Roll (°)	Pitch (°)	Yaw (°)
RMS	0.701	0.197	0.908	1.360	1.600	0.244

5. Simulation Studies

Four scenarios were examined in simulation, all tracking the trajectories given in equations (97)-(99) in the presence of the six-DOF, sea state 6 ship motion. The first scenario featured no additional disturbance, while in the second scenario a 0.5 second impulse was applied on both the x and y axes of the payload. The third scenario examined the effect of uncertain actuator dynamics and mass values on the system's performance, and the fourth scenario examined the behavior of the self-tuning parameters.

5.1. Scenario 1: No additional disturbance

Figure 11 shows the performance of the seven-DOF knuckle boom crane tracking the desired trajectory given in equations (97)-(99) with no additional disturbances. In Figure 11: the solid black line shows the desired x, y, z and cable length trajectories; the dotted line with diamond markers shows the performance of the system without the anti-sway trajectory modifier; the solid line with circle markers shows the performance of the system with the anti-sway trajectory modifier, but with static gains ξ_x, ξ_y, ξ_z and ξ_l; and the solid gray line shows the performance of the system with the self-tuning anti-sway trajectory modifier. With static gains, the anti-sway trajectory modifier provides a reduction of 63% in RMSE between the desired and actual payload positions when averaged across the x and y trajectories. The change in RMSE in the z and cable length trajectories are on the order of millimetres and are considered negligible. With self-tuning enabled, the anti-sway trajectory modifier provides an average reduction of 73% across the x and y trajectories compared to the performance without the trajectory modifier. Figure 12 shows the last 10 seconds of the simulation in greater detail, and demonstrates the effectiveness of the self-tuning anti-sway trajectory modifier, particularly for the x trajectory; while the y trajectory is primarily actuated by the slew motor, the x trajectory is primarily actuated by both the jib actuator and the jib extension, and is susceptible to the optimizer switching between favouring one actuator over the other.

5.2. Scenario 2: Added Disturbance

To test the system against sudden disturbances, a 5 kN force was applied to the payload along both the x and y axes for 0.5 seconds. Tracking the trajectories given in equations (97)-(99), Figure 13 shows the response of the system both with and without the anti-sway trajectory modifier, and both with and without the self-tuning enabled; the disturbance is applied at $t = 50$ seconds, and the RMSE is calculated from 60-100 seconds. Figure 14 shows the performance of the system between 60-100 seconds of the simulation. While the disturbance initially causes large errors in the payload position, the control system significantly dampens the oscillations after 10-15 seconds. Considering only the payload position RMSE from 60 to 100 seconds, the addition of the anti-sway trajectory modifier provides an average reduction in RMSE of 55% across the x and y trajectories compared to the performance without the trajectory modifier. Allowing the anti-sway trajectory modifier to self-tune provides an average reduction in RMSE of 77% between the x and y trajectories compared to without the trajectory modifier.

5.3. Scenario 3: Uncertain Actuator and Mass Parameters

In the previous scenarios, the model parameters used in the SMC were identical to the parameters in the digital twin. Practically, the masses of the crane components may not be exactly known, and added mass may be present in the form of piping, electrical boxes and paint; additionally, the time constants of the actuator transfer functions may not be identified accurately. To test the robustness of the self-tuning anti-sway control system to such uncertainties, the mass and elements of the inertia matrices of every rigid body in the digital twin were varied from $\pm20\%$ compared to the baseline (or ideal) case. The time constants of the actuator transfer functions were also varied from -20%, representing actuators with a faster response time than the baseline case, up to +20%, representing actuators with a slower response time than the baseline case. For each test, the parameters were only changed in the digital twin; the SMC calculated

the control action using only the parameters from the baseline case. The remaining test conditions are the same as those used in scenario 1.

Table 5 shows the percent change in RMSE, averaged across all four trajectories, as the parameters in the digital twin were varied away from the baseline case. The black numbers represent the percent change in RMSE when the anti-sway trajectory modifier self-tuned, while the grey numbers in brackets represent the percent change in RMSE with static gains in the trajectory modifier. The relatively consistent bracket values in each column of Table 5 show that the SMC alone is robust to errors in the actuator time constants. However, the relatively consistent black values across each row show that the self-tuning anti-sway trajectory modifier provides substantial improvements in performance due to errors in the mass parameters—a maximum error of 6.3% across all test cases, compared to the maximum error of 56% with static gains.

5.4. Scenario 4: Examination of the Self-Tuning Parameters

To demonstrate the strength of allowing the anti-sway trajectory modifier to self-tune, the left-hand side of Figure 15 shows the temporal evolution of the self-tuning gains ξ_x and ξ_y with the nominal trajectory given in equations 97–99 for four cases: in the first case, both the SMC and digital twin use the ideal parameters; in the second case, the digital twin has a +20% error in both the mass/inertial parameters and actuator time constants; in the third case, both the SMC and digital twin use the ideal parameters, while the same disturbance used in scenario 2 is applied to the payload at $t = 50$ seconds; in the fourth case, the digital twin has a +20% error in both the mass/inertial parameters and actuator time constants, and with the disturbance applied at $t = 50$ seconds. The right-hand side of Figure 15 shows the evolution of the self-tuning offsets ξ_z and ξ_l for the same four scenarios. Within the first 50 seconds of Figure 15 the variation of ξ_x and ξ_y is quite pronounced; the variation is related to the time-varying trajectories, which continue to change for the first 35 seconds of the simulation. The ability of the gains to self-tune while the trajectories vary removes the need for the gains to be scheduled, tuned, or designed for specific operating conditions.

For all test cases shown in Figure 15, once the system reaches steady-state (at approximately $t > 60$ seconds) all four self-tuning parameters approach and oscillate around a constant value. In the disturbance tests, a small deviation is observed in the ξ_x values when the disturbance is applied; no appreciable deviation is noticed in the ξ_y. To help visualize the deviation the left-hand side of Figure 16 provides a zoomed view of the evolution of ξ_x. The deviation of ξ_x due to the disturbance helped the anti-sway trajectory modifier reduce undesired payload motion, as seen in scenario 2. For both ξ_x and ξ_y the +20% parameter error resulted in only a small deviation between the gain values of the ideal case.

The right-hand side of Figures 15 and 16 shows the evolution of the self-tuning offsets ξ_z and ξ_l; when the disturbance was applied at $t = 50$ seconds, the system compensated with a relatively rapid change in both ξ_z and ξ_l, shown by the large spikes. For the cases with the +20% parameter errors, ξ_z and ξ_l compensated for the additional mass by self-tuning away from the ideal zero value, reducing the effect of the extra mass on system performance. The combined actions of the self-tuning parameters ξ_x, ξ_y, ξ_z and ξ_l resulted in the noticeable improvement in the system performance for the time-varying trajectories, disturbance rejection and compensation for the errors in the system parameters.

A final series of tests were performed to further highlight the ability of the self-tuning parameters to improve system performance with time-varying trajectories. The first test removed the time-varying trajectory completely, commanding the crane to maintain the payload's initial position, while the second, third and fourth tests multiplied the trajectories given in equations (97)-(99) by 0.5, 1.0 (the nominal trajectory) and 1.5, respectively. The performance with each trajectory was evaluated both with the ideal parameters in the digital twin and with +20% error in the mass/inertial parameters and actuator time constants. Table 6 provides the mean and standard deviation of all four self-tuning parameters for each test, along with the average RMSE across all four trajectories, both with the self-tuning anti-sway trajectory modifier and without any trajectory modification for comparison. The rows of Table 6 show a significant change in the mean values of the ξ_x and ξ_y gains, indicating the system was compensating for the various trajectories, while the ξ_z and ξ_l offsets remain relatively constant. Evaluated over the final 50 seconds of each test, the means of each gain remain fairly constant given the relatively small standard deviations. For the tests with +20% parameter error, the mean values of the offsets ξ_z and ξ_l self-tune to compensate for the extra mass, while and the gains ξ_x and ξ_y remain relatively unchanged from the ideal case. The results indicate that ξ_x and ξ_y primarily compensate for variations in the trajectory, while ξ_z and ξ_l primarily compensate for variations in the system parameters. The self-tuning gains provided up to a 92% reduction in the average RMSE compared to the performance without anti-sway trajectory modification, with a minimum reduction of 77%—still a considerable improvement.

Table 5
Percent change in average RMSE across all four trajectories with uncertain mass parameters and actuator time constants τ_i. The black numbers represent the percent change in RMSE with self-tuning enabled for the anti-sway trajectory modifier, while the gray numbers in brackets represent the percent change in RMSE with self-tuning disabled (static gains).

Percent Change in RMSE vs **Baseline** with Self-Tuning (Without Self-Tuning)			Percent Change in Mass and Inertial Parameters				
			← *Lighter*		**Baseline**	*Heavier* →	
			−20%	−10%	**0%**	+10%	+20%
	↑	−20%	+6.3% (+55%)	+3.1% (+40%)	−0.1% (+25%)	−1.9% (+44%)	−4.9% (+56%)
Percent	*Faster*	−10%	+3.4% (+53%)	+3.1% (+40%)	+0.2% (+25%)	−1.8% (+44%)	−4.7% (+56%)
Change	**Baseline**	**0%**	+3.5% (+53%)	+3.1% (+40%)	− − − (+25%)	−2.0% (+44%)	−4.7% (+56%)
in τ_i	*Slower*	+10%	+3.4% (+53%)	+3.2% (+40%)	+0.4% (+25%)	−2.1% (+44%)	−4.5% (+56%)
	↓	+20%	+3.7% (+53%)	+3.2% (+40%)	+0.4% (+25%)	−2.1% (+44%)	−4.4% (+56%)

Table 6
The mean and standard deviation of the four self-tuning parameters for tests with different time-varying trajectories, along with the corresponding RMSE averaged across all four trajectories. Tests were performed both with the ideal mass/inertial parameters and actuator time constants in the digital twin, and with +20% error in these parameters. *No Trajectory* refers to when the crane is commanded to maintain the payload's initial position, *0.5 Trajectory* refers to a trajectory that is half the speed of the nominal trajectory, *Nominal Trajectory* refers to the trajectory given in equations (97)-(99), and *1.5 Trajectory* refers to a trajectory that is one-and-a-half times the nominal trajectory. *Anti-Sway* refers to results obtained with the self-tuning anti-sway trajectory modifier, while *No Anti-Sway* refers to results obtained without any trajectory modification for comparison. All simulations were run for 200 seconds, and the means and standard deviations were evaluated over the final 50 seconds.

Ideal digital twin: No errors in mass/inertial parameters or actuator time constants

	No Trajectory	0.5 Trajectory	Nominal Trajectory	1.5 Trajectory
Self-Tuning Parameters	*Mean ± std*	*Mean ± std*	*Mean ± std*	*Mean ± std*
ξ_x	0.729 ± 0.006	0.689 ± 0.008	0.631 ± 0.007	0.593 ± 0.007
ξ_y	1.105 ± 0.009	1.085 ± 0.010	1.070 ± 0.010	1.071 ± 0.009
ξ_z	0.001 ± 0.001	0.000 ± 0.001	0.000 ± 0.002	0.001 ± 0.005
ξ_l	-0.001 ± 0.000	-0.001 ± 0.000	-0.001 ± 0.000	-0.001 ± 0.000
RMSE				
Average *(No Anti-Sway)*	0.060 m	0.071 m	0.084 m	0.099 m
Average *(Anti-Sway)*	0.005 m	0.008 m	0.013 m	0.019 m
% Reduction	**92**%	**89**%	**85**%	**81**%

+20% error in the mass/inertial parameters and actuator time constants in the digital twin

|	No Trajectory	0.5 Trajectory	Nominal Trajectory	1.5 Trajectory
Self-Tuning Parameters	*Mean ± std*	*Mean ± std*	*Mean ± std*	*Mean ± std*
ξ_x	0.805 ± 0.015	0.668 ± 0.009	0.632 ± 0.011	0.610 ± 0.022
ξ_y	1.118 ± 0.009	1.095 ± 0.010	1.084 ± 0.010	1.086 ± 0.009
ξ_z	0.072 ± 0.002	0.072 ± 0.002	0.071 ± 0.0021	0.077 ± 0.0079
ξ_l	-0.009 ± 0.000	-0.009 ± 0.000	-0.009 ± 0.000	-0.009 ± 0.000
RMSE				
Average *(No Anti-Sway)*	0.080 m	0.091 m	0.104 m	0.119 m
Average *(Anti-Sway)*	0.009 m	0.007 m	0.012 m	0.028 m
% Reduction	**89**%	**92**%	**88**%	**77**%
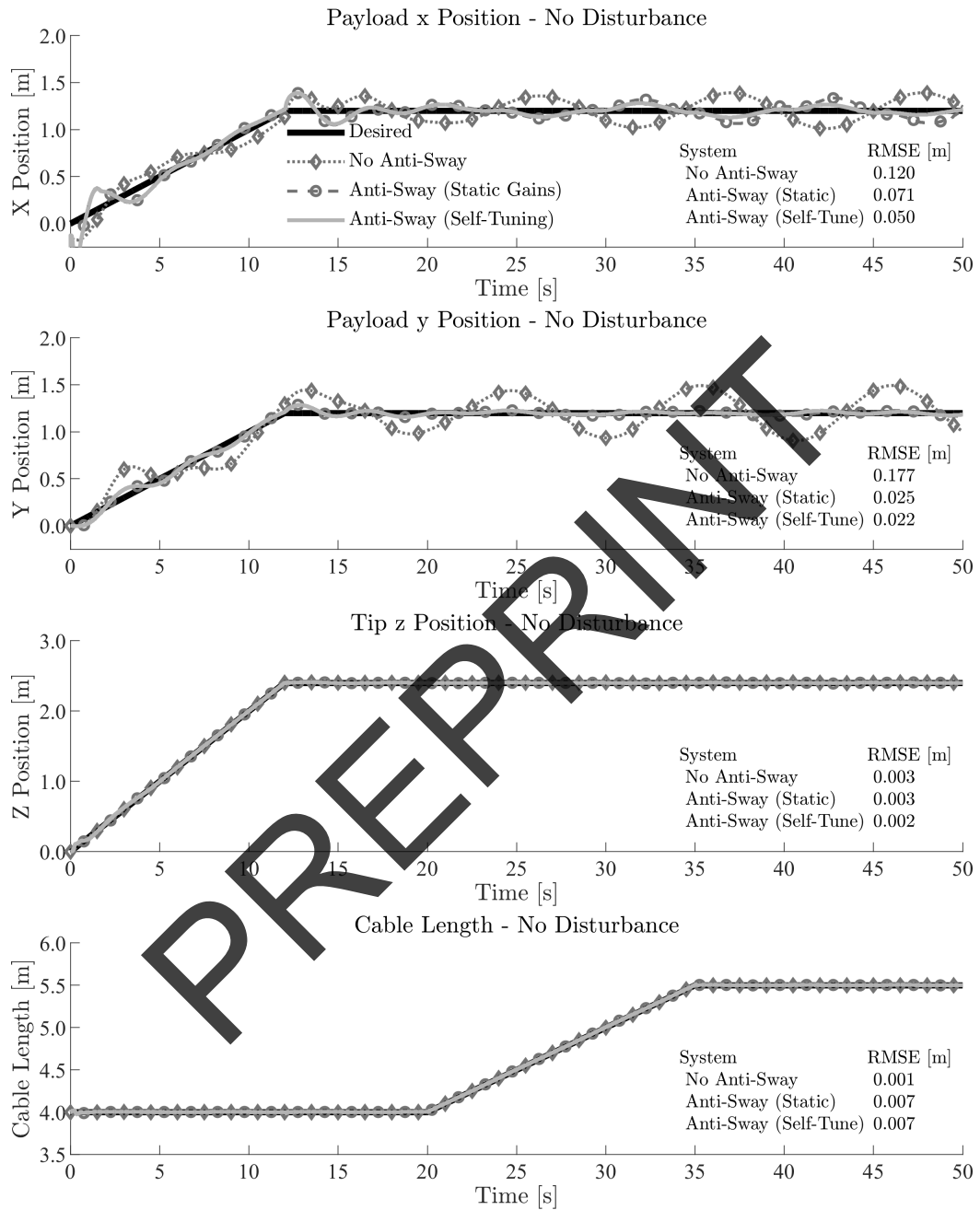
Figure 11: Tracking performance of the 7-DOF knuckle boom crane both with and without self-tuning anti-sway trajectory modification. *No Anti-Sway* refers to performance without the anti-sway trajectory modifier, *Anti-Sway (Static)* refers to performance with the anti-sway trajectory modifier but without self-tuning (static gains), while *Anti-Sway (Self-Tune)* refers to performance where the anti-sway trajectory modifier utilizes self-tuning. RMSE was calculated only using data after the first 5 seconds of the simulation to allow for initialization.
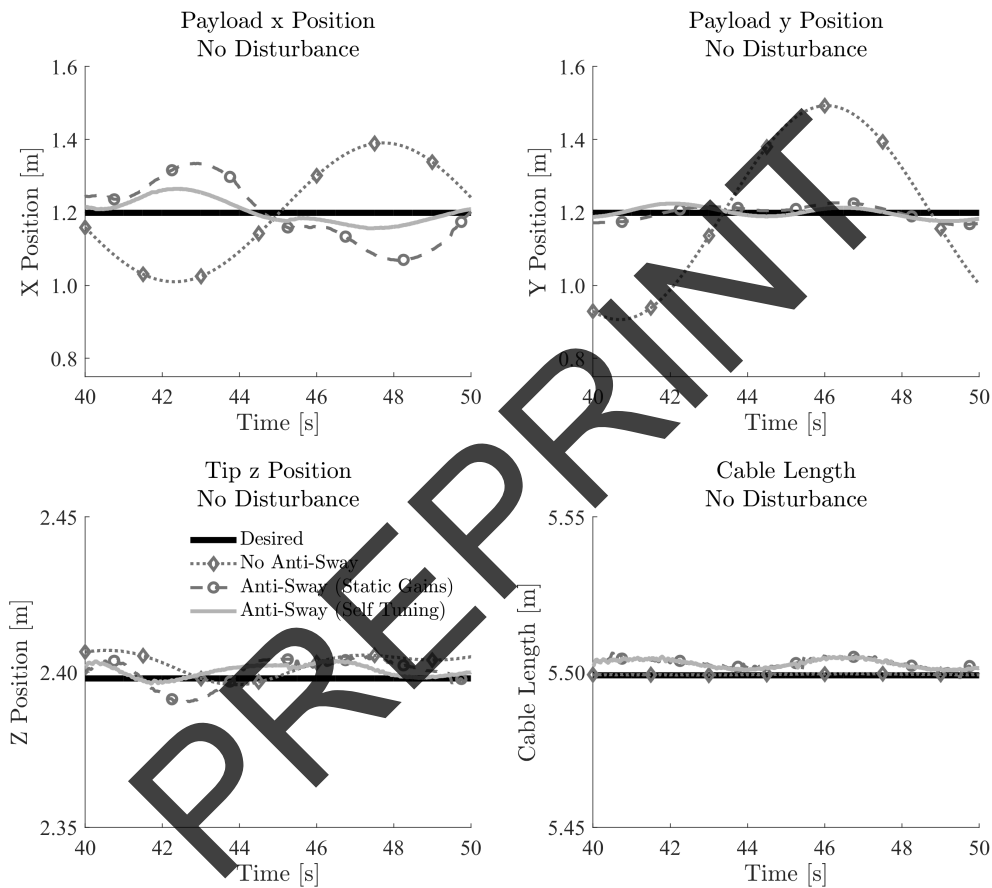
Figure 12: The final ten seconds of the no-disturbance simulation, showing the improvement in tracking with the self-tuning anti-sway trajectory modifier.
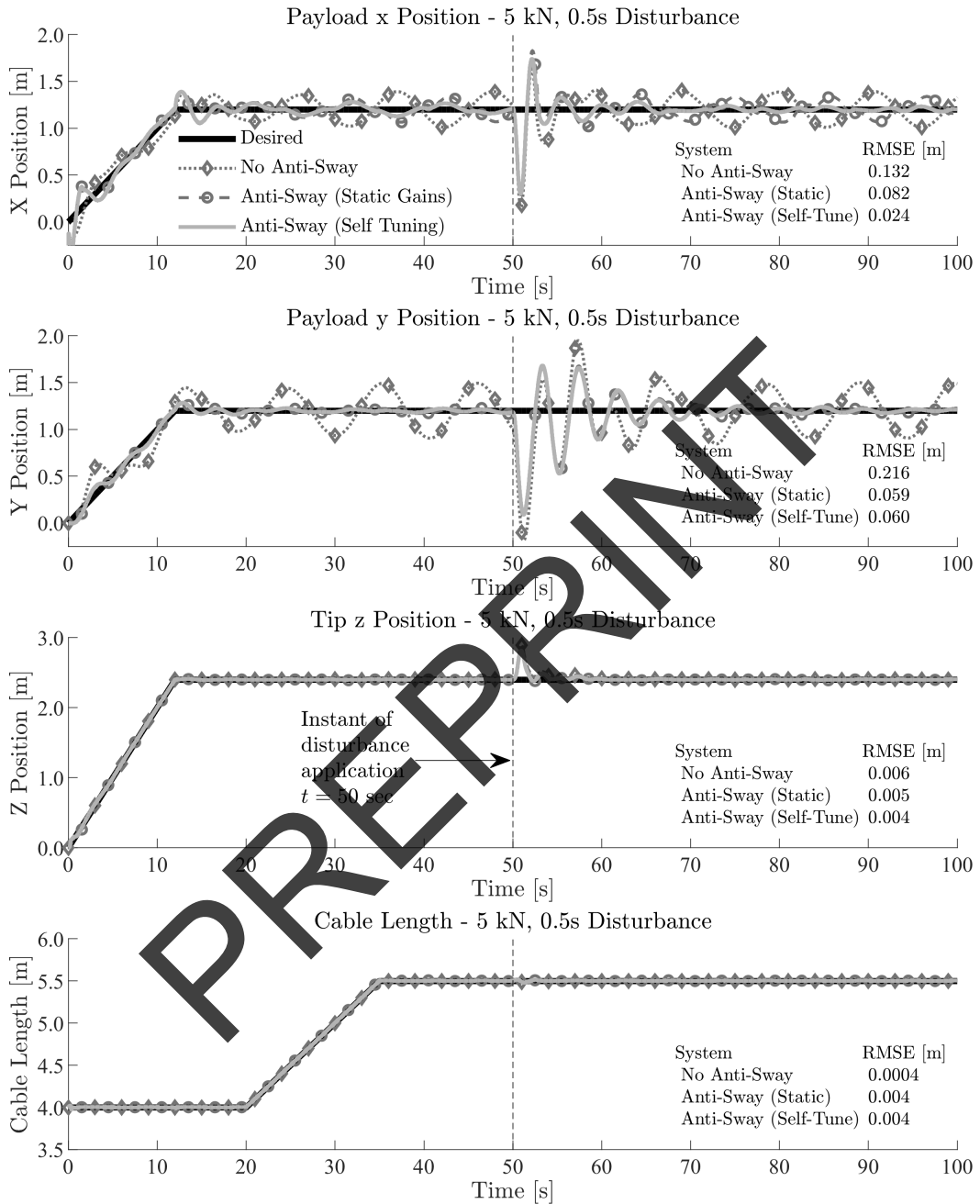
Figure 13: Tracking performance of the 7-DOF knuckle boom crane in the presence of a 5 kN disturbance applied at a simulation time of 50 seconds for a duration of 0.5 seconds. *No Anti-Sway* refers to no anti-sway trajectory modification, *Anti-Sway (Static)* refers to with the anti-sway trajectory modifier but with static gains, and *Anti-Sway (Self-Tune)* refers to the self-tuning anti-sway trajectory modifier. The dashed line indicates the time at which the disturbance is applied to the payload.
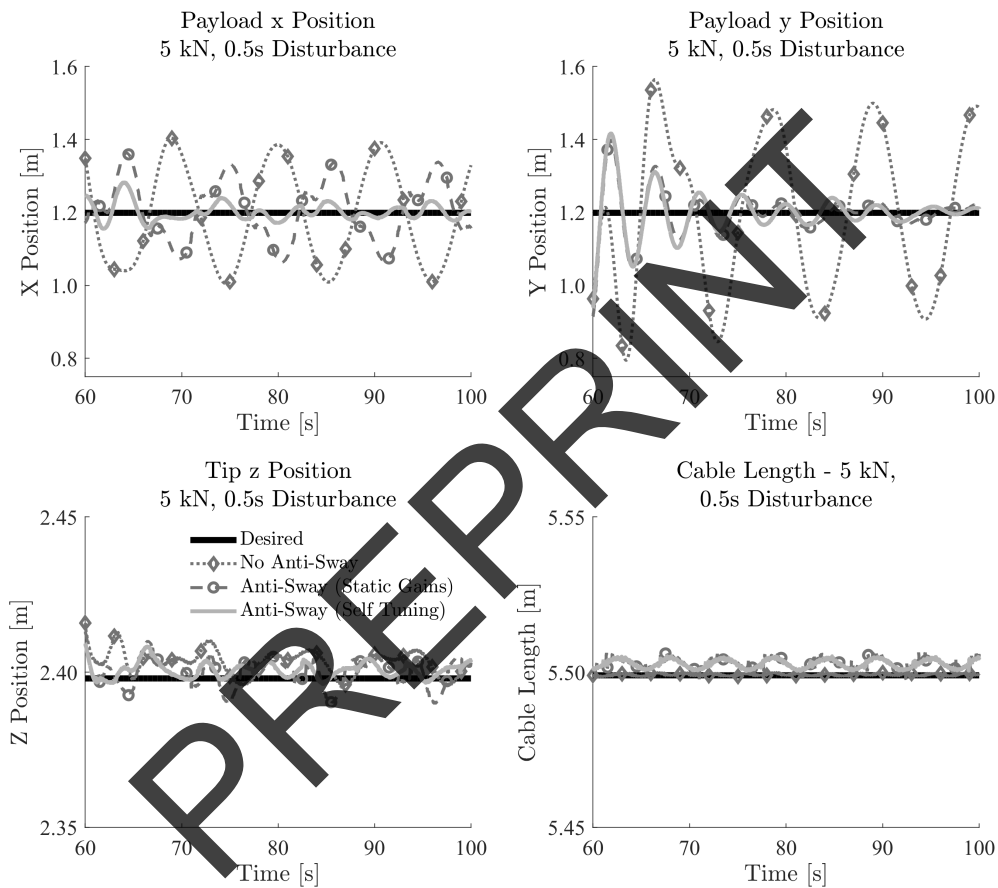
Figure 14: The final forty seconds of the disturbance simulation, showing the disturbance rejection performance of the self-tuning anti-sway trajectory modifier.
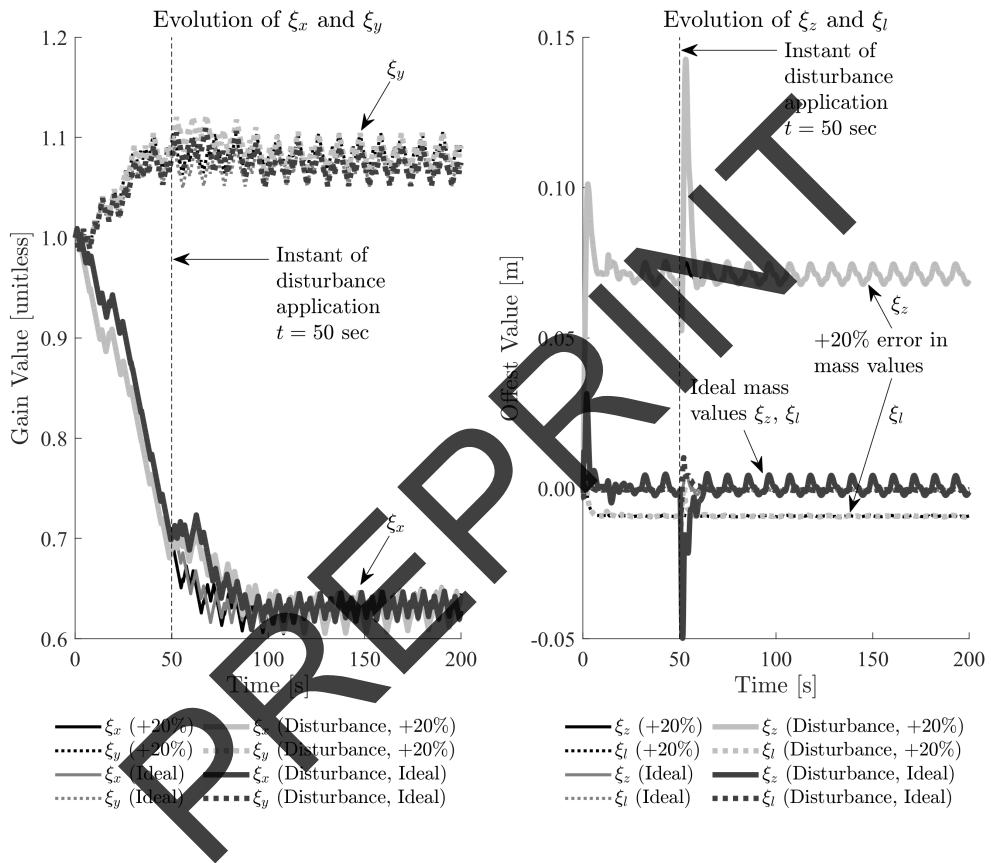
Figure 15: The evolution of the self-tuning gains ξ_x, ξ_y, ξ_z and ξ_l over an extended 200 second test for cases with and without the applied disturbance for a crane system with ideal parameters and a +20% parameter error.
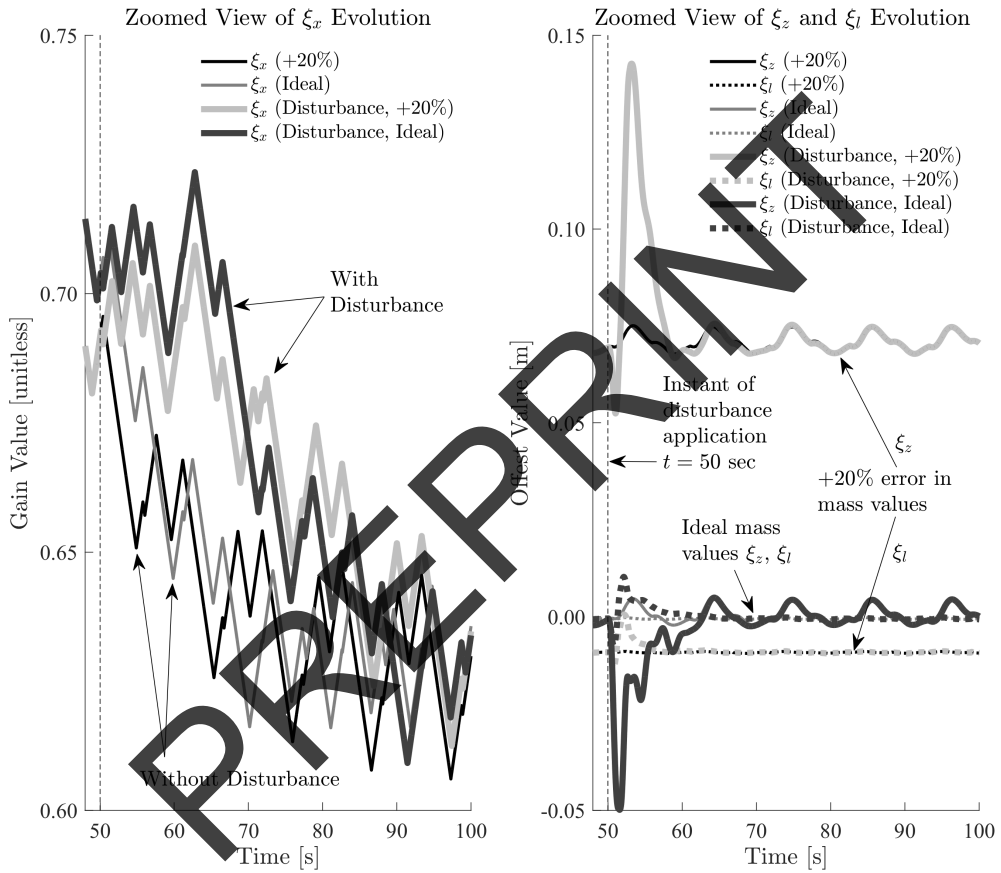
Figure 16: The evolution of the self-tuning gains ξ_x, ξ_y, ξ_z and ξ_l between 50 and 100 seconds for cases with and without the applied disturbance for a crane system with ideal parameters and a +20% parameter error.

6. Conclusion

In this paper a dynamic model and anti-sway control system are developed for a seven-DOF shipboard knuckle boom crane, helping to address the lack of research in anti-sway control for high-DOF shipboard cranes. The dynamic model was developed to improve the model fidelity beyond what is typically seen in literature and includes the mass and inertia of the actuators, sheaves and winch, internal actuator dynamics and a realistic cable fall angle. The equations of motion of the dynamic model were derived using the Lagrange approach to provide stable control of the seven-DOF knuckle boom crane with an SMC. The kinematics of the knuckle boom crane were derived using both the standard transformation matrix approach as well as with dual quaternions. When computed using Maple, the equations of motion code for the dual quaternions was 30% shorter than the code produced using the transformation matrices, reducing the computational cost of the SMC when deployed to hardware.

To provide anti-sway control, a self-tuning anti-sway trajectory modifier was developed for the crane and implemented in combination with the SMC. A nonlinear trajectory optimizer was built to allow the crane to track the desired trajectory using all five actuators. When tested with six-DOF ship motion, it was found through simulation that with static gains, the anti-sway trajectory modifier provided a 63% reduction in RMSE between the desired and actual payload positions averaged across the x and y trajectories, compared to the performance without the anti-sway trajectory modifier. With self-tuning enabled, the anti-sway trajectory modifier showed a 73% reduction in RMSE across the x and y trajectories compared to the case without the modifier. Applying a 5 kN disturbance force in both the x and y directions to the payload, the anti-sway trajectory modifier with static gains showed a 56% reduction in RMSE compared to without the modifier, while with self-tuning enabled showed a 77% reduction in RMSE compared to without the modifier.

To test the robustness of the self-tuning anti-sway control system, the mass/inertial parameters and actuator time constants of the digital twin, the stand-in for a physical knuckle boom crane, were varied by $\pm 20\%$ away from the baseline values used by the SMC in the anti-sway control system. With self-tuning enabled, the maximum increase in RMSE averaged across all four trajectories was only 6.3% above the baseline performance, while with self-tuning disabled and the gains held static, the maximum increase in average RMSE was 56%. When tested with different time-varying trajectories, the self-tuning anti-sway trajectory modifier showed up to a 92% reduction in average RMSE compared to the case without the modifier; the minimum reduction in RMSE was 77%, corresponding to a simulation with +20% error in both mass/inertial parameters and actuator time constants, and with the fastest trajectory tested.

The results therefore indicate that the anti-sway control system for the seven-DOF shipboard knuckle boom crane, built using a self-tuning trajectory modifier and an SMC is highly effective at reducing undesired payload motion along time-varying trajectories, and is robust to both sudden disturbances and parameter uncertainties.

A. Position Kinematics with Transformation Matrices

Using the DH parameters presented in Tables 1, 2 and 3, transformation matrices between each coordinate frame can be populated with equation (4). For the main kinematic chain, the transformation matrices are

$$
{}^{D}T_1 = \begin{bmatrix} \cos(\theta_0) & 0 & -\sin(\theta_0) & 0 \\ \sin(\theta_0) & 0 & \cos(\theta_0) & 0 \\ 0 & -1 & 0 & l_0 \\ 0 & 0 & 0 & 1 \end{bmatrix},
\tag{100}
$$

$$
{}^{1}T_2 = \begin{bmatrix} \cos(\theta_1) & -\sin(\theta_1) & 0 & l_1\cos(\theta_1) \\ \sin(\theta_1) & \cos(\theta_1) & 0 & l_1\sin(\theta_1) \\ 0 & 0 & 1 & 0 \\ 0 & 0 & 0 & 1 \end{bmatrix}, \tag{101}
$$

$$
{}^{2}T_3 = \begin{bmatrix} \cos(\theta_2) & -\sin(\theta_2) & 0 & l_2\cos(\theta_2) \\ \sin(\theta_2) & \cos(\theta_2) & 0 & l_2\sin(\theta_2) \\ 0 & 0 & 1 & 0 \\ 0 & 0 & 0 & 1 \end{bmatrix}, \tag{102}
$$

$$
{}^{3}T_4 = \begin{bmatrix} 1 & 0 & 0 & d_3 \\ 0 & 1 & 0 & 0 \\ 0 & 0 & 1 & 0 \\ 0 & 0 & 0 & 1 \end{bmatrix}, \tag{103}
$$

$$
{}^{4}T_5 = \begin{bmatrix} 0 & 1 & 0 & 0 \\ -1 & 0 & 0 & -l_4 \\ 0 & 0 & 1 & 0 \\ 0 & 0 & 0 & 1 \end{bmatrix}, \tag{104}
$$

$$
{}^{5}T_6 = \begin{bmatrix} \cos(\theta_5) & -\sin(\theta_5) & 0 & r_2\cos(\theta_5) \\ \sin(\theta_5) & \cos(\theta_5) & 0 & r_2\sin(\theta_5) \\ 0 & 0 & 1 & 0 \\ 0 & 0 & 0 & 1 \end{bmatrix}, \tag{105}
$$

$$
{}^{6}T_7 = \begin{bmatrix} \cos(\theta_6) & 0 & \sin(\theta_6) & 0 \\ \sin(\theta_6) & 0 & -\cos(\theta_6) & 0 \\ 0 & 1 & 0 & 0 \\ 0 & 0 & 0 & 1 \end{bmatrix}, \tag{106}
$$

$$
{}^{7}T_8 = \begin{bmatrix} \cos(\theta_7) & -\sin(\theta_7) & 0 & 0 \\ \sin(\theta_7) & \cos(\theta_7) & 0 & 0 \\ 0 & 0 & 1 & 0 \\ 0 & 0 & 0 & 1 \end{bmatrix}, \tag{107}
$$

$$
{}^{8}T_9 = \begin{bmatrix} 1 & 0 & 0 & l_8 \\ 0 & 1 & 0 & 0 \\ 0 & 0 & 1 & 0 \\ 0 & 0 & 0 & 1 \end{bmatrix}. \tag{108}
$$

Likewise for the boom actuator kinematic chain the transformation matrices are

$$
{}^{D}T_{b1} = \begin{bmatrix} \cos(\theta_0) & 0 & -\sin(\theta_0) & 0 \\ \sin(\theta_0) & 0 & \cos(\theta_0) & 0 \\ 0 & -1 & 0 & 0 \\ 0 & 0 & 0 & 1 \end{bmatrix}, \tag{109}
$$

$$
{}^{b1}T_{b2} = \begin{bmatrix} \cos(\theta_{b1}) & -\sin(\theta_{b1}) & 0 & l_{b1}\cos(\theta_{b1}) \\ \sin(\theta_{b1}) & \cos(\theta_{b1}) & 0 & l_{b1}\sin(\theta_{b1}) \\ 0 & 0 & 1 & 0 \\ 0 & 0 & 0 & 1 \end{bmatrix}, \tag{110}
$$

$$
{}^{b2}T_{b3} = \begin{bmatrix} \cos(\theta_{b2}) & -\sin(\theta_{b2}) & 0 & l_{b2}\cos(\theta_{b2}) \\ \sin(\theta_{b2}) & \cos(\theta_{b2}) & 0 & l_{b2}\sin(\theta_{b2}) \\ 0 & 0 & 1 & 0 \\ 0 & 0 & 0 & 1 \end{bmatrix}, \tag{111}
$$

$$
{}^{b3}T_{b4} = \begin{bmatrix} 1 & 0 & 0 & d_1 \\ 0 & 1 & 0 & 0 \\ 0 & 0 & 1 & 0 \\ 0 & 0 & 0 & 1 \end{bmatrix}. \tag{112}
$$

Finally for the jib actuator kinematic chain the transformation matrices are

$$
{}^{1}T_{c1} = \begin{bmatrix} \cos(\theta_{c1}) & -\sin(\theta_{c1}) & 0 & l_{c1}\cos(\theta_{c1}) \\ \sin(\theta_{c1}) & \cos(\theta_{c1}) & 0 & l_{c1}\sin(\theta_{c1}) \\ 0 & 0 & 1 & 0 \\ 0 & 0 & 0 & 1 \end{bmatrix}, \tag{113}
$$

$$
{}^{c1}T_{c2} = \begin{bmatrix} \cos(\theta_{c2}) & -\sin(\theta_{c2}) & 0 & l_{c2}\cos(\theta_{c2}) \\ \sin(\theta_{c2}) & \cos(\theta_{c2}) & 0 & l_{c2}\sin(\theta_{c2}) \\ 0 & 0 & 1 & 0 \\ 0 & 0 & 0 & 1 \end{bmatrix}, \tag{114}
$$

$$
{}^{c2}T_{c3} = \begin{bmatrix} 1 & 0 & 0 & d_2 \\ 0 & 1 & 0 & 0 \\ 0 & 0 & 1 & 0 \\ 0 & 0 & 0 & 1 \end{bmatrix}. \tag{115}
$$

With transformation matrices defined between the joints in the knuckle boom crane, the kinematics of the centres of gravity of each rigid body can be defined. Using the geometry shown in Figure 3, the centre of gravity of the base can be written with respect to $(XYZ)_1$ as

$$
{}^{1}T_{cog0} = \begin{bmatrix} 1 & 0 & 0 & -l_{cog0,x} \\ 0 & 1 & 0 & l_{cog0,y} \\ 0 & 0 & 1 & 0 \\ 0 & 0 & 0 & 1 \end{bmatrix}. \tag{116}
$$

Likewise the centres of gravity of the boom, jib and extension can be written with respect to coordinate frames $(XYZ)_2$, $(XYZ)_3$ and $(XYZ)_4$, respectively, as

$$
{}^{2}T_{cog1} = \begin{bmatrix} 1 & 0 & 0 & -l_{cog1,x} \\ 0 & 1 & 0 & -l_{cog1,y} \\ 0 & 0 & 1 & 0 \\ 0 & 0 & 0 & 1 \end{bmatrix}, \quad {}^{3}T_{cog2} = \begin{bmatrix} 1 & 0 & 0 & -l_{cog2,x} \\ 0 & 1 & 0 & -l_{cog2,y} \\ 0 & 0 & 1 & 0 \\ 0 & 0 & 0 & 1 \end{bmatrix}, \quad {}^{4}T_{cog3} = \begin{bmatrix} 1 & 0 & 0 & -l_{cog3,x} \\ 0 & 1 & 0 & -l_{cog3,y} \\ 0 & 0 & 1 & 0 \\ 0 & 0 & 0 & 1 \end{bmatrix}. \tag{117}
$$

The centres of gravity of the winch and the boom sheave with respect to coordinate frame $(XYZ)_2$ and the jib sheave with respect to $(XYZ)_3$ are given by

$$
{}^{2}T_{w} = \begin{bmatrix} 1 & 0 & 0 & -l_{w,x} \\ 0 & 1 & 0 & -l_{w,y} \\ 0 & 0 & 1 & 0 \\ 0 & 0 & 0 & 1 \end{bmatrix}, \quad {}^{2}T_{s0} = \begin{bmatrix} 1 & 0 & 0 & -l_{s0,x} \\ 0 & 1 & 0 & -l_{s0,y} \\ 0 & 0 & 1 & 0 \\ 0 & 0 & 0 & 1 \end{bmatrix}, \quad {}^{3}T_{s1} = \begin{bmatrix} 1 & 0 & 0 & -l_{s1,x} \\ 0 & 1 & 0 & -l_{s1,y} \\ 0 & 0 & 1 & 0 \\ 0 & 0 & 0 & 1 \end{bmatrix}. \tag{118}
$$

Note that the centres of gravity of the final sheave and the payload are located at coordinate frames $(XYZ)_5$ and $(XYZ)_9$, respectively. The centres of gravity of the boom actuator cylinder with respect to $(XYZ)_{b3}$ and the boom actuator rod with respect to $(XYZ)_{b4}$ are

$$
{}^{b3}T_{cogb1} = \begin{bmatrix} 1 & 0 & 0 & -l_{cogb1} \\ 0 & 1 & 0 & 0 \\ 0 & 0 & 1 & 0 \\ 0 & 0 & 0 & 1 \end{bmatrix}, \quad {}^{b4}T_{cogb2} = \begin{bmatrix} 1 & 0 & 0 & -l_{cogb2} \\ 0 & 1 & 0 & 0 \\ 0 & 0 & 1 & 0 \\ 0 & 0 & 0 & 1 \end{bmatrix}. \tag{119}
$$

The centres of gravity of the jib actuator cylinder with respect to $(XYZ)_{c2}$ and the boom actuator rod with respect to $(XYZ)_{c3}$ are

$$
^{c2}T_{cogc1} = \begin{bmatrix} 1 & 0 & 0 & -l_{cogc1} \\ 0 & 1 & 0 & 0 \\ 0 & 0 & 1 & 0 \\ 0 & 0 & 0 & 1 \end{bmatrix}, \quad ^{c3}T_{cogc2} = \begin{bmatrix} 1 & 0 & 0 & -l_{cogc2} \\ 0 & 1 & 0 & 0 \\ 0 & 0 & 1 & 0 \\ 0 & 0 & 0 & 1 \end{bmatrix}. \tag{120}
$$

Therefore, the transformation matrices describing the kinematics of each centre of gravity with respect to the deck coordinate frame can be written as concatenations of the transformation matrices given in equations (100)-(120),

$$
^{D}T_{cog0} = {}^{D}T_1 {}^{1}T_{cog0}, \tag{121}
$$

$$
^{D}T_{cog1} = {}^{D}T_1 {}^{1}T_2 {}^{2}T_{cog1}, \tag{122}
$$

$$
^{D}T_{cog2} = {}^{D}T_1 {}^{1}T_2 {}^{2}T_3 {}^{3}T_{cog2}, \tag{123}
$$

$$
^{D}T_{cog3} = {}^{D}T_1 {}^{1}T_2 {}^{2}T_3 {}^{3}T_{cog3}, \tag{124}
$$

$$
^{D}T_{w} = {}^{D}T_1 {}^{1}T_2 {}^{2}T_{w}, \tag{125}
$$

$$
^{D}T_{s0} = {}^{D}T_1 {}^{1}T_2 {}^{2}T_{s0}, \tag{126}
$$

$$
^{D}T_{s1} = {}^{D}T_1 {}^{1}T_2 {}^{2}T_3 {}^{3}T_{s1}, \tag{127}
$$

$$
^{D}T_{s2} = {}^{D}T_1 {}^{1}T_2 {}^{2}T_3 {}^{3}T_4 {}^{4}T_5, \tag{128}
$$

$$
^{D}T_{pay} = {}^{D}T_1 {}^{1}T_2 {}^{2}T_3 {}^{3}T_4 {}^{4}T_5 {}^{5}T_6 {}^{6}T_7 {}^{7}T_8 {}^{8}T_9, \tag{129}
$$

$$
^{D}T_{cogb1} = {}^{D}T_{b1} {}^{b1}T_{b2} {}^{b2}T_{b3} {}^{b3}T_{cogb1}, \tag{130}
$$

$$
^{D}T_{cogb2} = {}^{D}T_{b1} {}^{b1}T_{b2} {}^{b2}T_{b3} {}^{b3}T_{b4} {}^{b4}T_{cogb2}, \tag{131}
$$

$$
^{D}T_{cogc1} = {}^{D}T_1 {}^{1}T_{c1} {}^{c1}T_{c2} {}^{c2}T_{cogc1}, \tag{132}
$$

$$
^{D}T_{cogc2} = {}^{D}T_1 {}^{1}T_{c1} {}^{c1}T_{c2} {}^{c2}T_{c3} {}^{c3}T_{cogc2}. \tag{133}
$$

The transformation matrix for centre of gravity i contains a 3×3 rotation matrix $^{D}R_i$ that describes the orientation of i with respect to the deck coordinate frame, and a 3×1 position vector $^{D}\vec{p}_i$ that describes the position of i with respect to the deck coordinate frame measured in the deck coordinate frame, as given in equation (3).

B. Intermediate Angles

The knuckle boom crane is actuated with the slew motor, rotating the base by an angle θ_0, and the hydraulic actuators extending distances d_1, d_2 and d_3. However, the kinematics of the knuckle boom crane are derived using intermediate angles θ_1, θ_2, θ_{b1}, θ_{b2}, θ_{c1} and θ_{c2}; expressions must be derived relating each intermediate angle to the actuator extensions d_1 and d_2.

Figure 17 shows the geometry required to express θ_1, θ_{b1} and θ_{b2} in terms of the actuator extension d_1. The intermediate lengths b_1 and b_4 are given as

$$
b_1 = \sqrt{l_{b1,x}^2 + (l_0 - l_{b1,z})^2}, \tag{134}
$$

$$
b_4 = \sqrt{l_{b4,x}^2 + l_{b4,y}^2}. \tag{135}
$$

With application of cosine law, the angles θ_1, θ_{b1} and θ_{b2} can be written as

$$
\theta_1 = \frac{\pi}{2} - \cos^{-1}\left(\frac{b_1^2 + b_4^2 - (d_1 + l_{b2})^2}{2 b_1 b_4} \right) - \tan^{-1}\left(\frac{l_{b1,x}}{l_0 - l_{b1,z}} \right) - \tan^{-1}\left(\frac{l_{b4,y}}{l_{b4,x}} \right), \tag{136}
$$

$$
\theta_{b1} = -\tan^{-1}\left(\frac{l_{b1,z}}{l_{b1,x}} \right), \tag{137}
$$
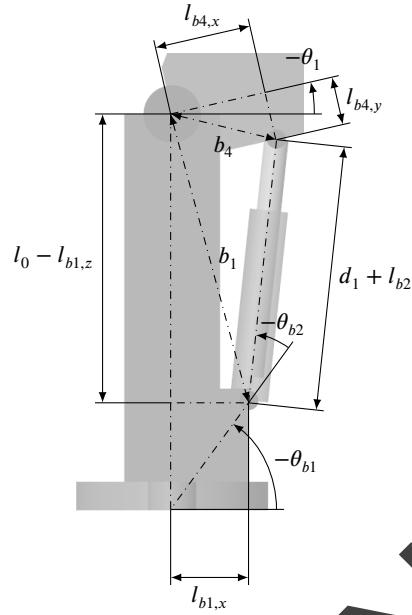
Figure 17: The geometry required to determine the intermediate angles θ_1, θ_{b1} and θ_{b2}.
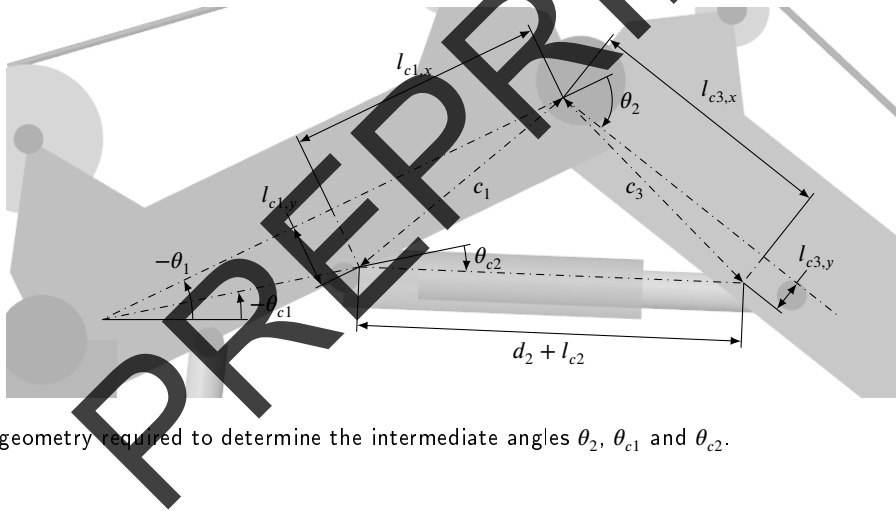
Figure 18: The geometry required to determine the intermediate angles θ_2, θ_{c1} and θ_{c2}.

$$\theta_{b2} = -\pi - \theta_{b1} + \cos^{-1}\left(\frac{b_1^2 + (d_1 + l_{b2})^2 - b_4^2}{2b_1(d_1 + l_{b2})}\right) + \cos^{-1}\left(\frac{l_{b1,x}}{b_1}\right) \tag{138}$$

Figure 18 shows the geometry required to express θ_2, θ_{c1} and θ_{c2} in terms of the actuator extension d_2. The intermediate lengths c_1 and c_3 are given as

$$c_1 = \sqrt{l_{c1,x}^2 + l_{c1,y}^2}, \tag{139}$$

$$c_2 = \sqrt{l_{c3,x}^2 + l_{c3,y}^2}. \tag{140}$$

The angles θ_2, θ_{c1} and θ_{c2} can then be written as

$$\theta_2 = \pi - \cos^{-1}\left(\frac{c_1^2 + c_3^2 - (d_2 + l_{c2})^2}{2c_1c_2}\right) - \tan^{-1}\left(\frac{l_{c1,y}}{l_{c1,x}}\right) - \tan^{-1}\left(\frac{l_{c3,y}}{l_{c3,x}}\right), \tag{141}$$

$$\theta_{c1} = \theta_1 + \tan^{-1}\left(\frac{l_{c1y}}{l_1 - l_{c1,x}}\right), \tag{142}$$

$$\theta_{c2} = -\frac{\pi}{2} - \tan^{-1}\left(\frac{l_{c1y}}{l_1 - l_{c1,x}}\right) + \cos^{-1}\left(\frac{c_1^2 + (d_2 + l_{c2})^2 - c_3^2}{2c_1(d_2 + l_{c2})}\right) + \tan^{-1}\left(\frac{l_{c1x}}{l_{c1y}}\right). \tag{143}$$

Note that θ_{c1} is a function of d_1 while θ_2 and θ_{c2} are only functions of d_2.

C. Cable Length

The length of cable by which the payload is hung below the final sheave is given by l_8. The additional cable running from the tip of the final sheave back to the winch l_c is only a function of the crane geometry. Using the geometry shown in Figure 19, the length of the cable l_{c0} spanning the winch and boom sheave can be found by first calculating the intermediate length l'_{c0},

$$l'_{c0} = \sqrt{(l_{w,x} - l_{s0,x})^2 + (l_{w,y} - l_{s0,y})^2}, \tag{144}$$

$$l_{c0} = \sqrt{(l'_{c0})^2 - (r_w - r_0)^2}, \tag{145}$$

and the cable entry angle α_0 is given by

$$\alpha_0 = \cos^{-1}\left(\frac{r_w - r_0}{l'_{c0}}\right) - \tan^{-1}\left(\frac{l_{w,y} - l_{s0,y}}{l_{w,x} - l_{s0,x}}\right). \tag{146}$$

Likewise, using the geometry shown in Figure 20, the length of the cable l_{c1} spanning the knuckle joint can be found by first calculating intermediate lengths l'_{s0} and l'_{s1},

$$l'_{s0} = \sqrt{l_{s0,x}^2 + l_{s0,y}^2}, \tag{147}$$

$$l'_{s1} = \sqrt{(l_2 - l_{s1,x})^2 + l_{s1,y}^2}. \tag{148}$$

The intermediate angle γ_1 and intermediate length l'_{c1} can then be calculated as

$$\gamma_1 = \pi + \theta_2 - \tan^{-1}\left(\frac{l_{s1,y}}{l_2 - l_{s1,x}}\right) - \tan^{-1}\left(\frac{l_{s0,y}}{l_{s0,x}}\right), \tag{149}$$

$$l'_{c1} = \sqrt{(l'_{s0})^2 + (l'_{s1})^2 - 2l'_{s0}l'_{s1}\cos(\gamma_1)}, \tag{150}$$

giving the cable length l_{c1} as

$$l_{c1} = \sqrt{(l'_{c1})^2 - (r_0 - r_1)^2}. \tag{151}$$

The cable exit angle β_0 and entry angle α_1 are given by

$$\beta_0 = -\frac{\pi}{2} + \cos^{-1}\left(\frac{(l'_{s0})^2 + (l'_{c1})^2 - (l'_{s1})^2}{2l'_{s0}l'_{c1}}\right) + \tan^{-1}\left(\frac{l_{s0,x}}{l_{s0,y}}\right) + \sin^{-1}\left(\frac{l_{c1}}{l'_{c1}}\right), \tag{152}$$
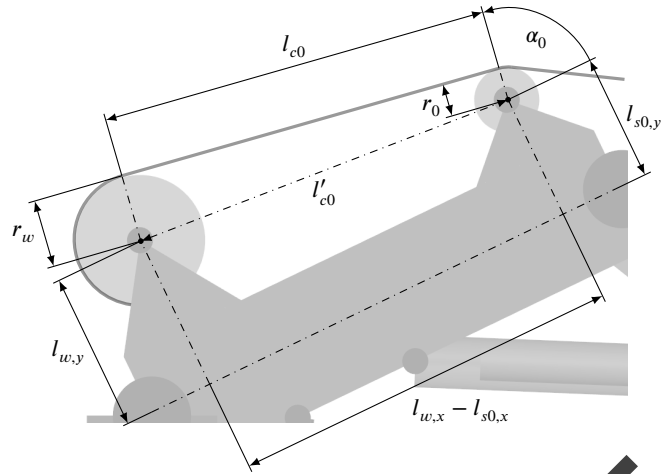
Figure 19: The geometry required to calculate the cable length between the winch and the first sheave.
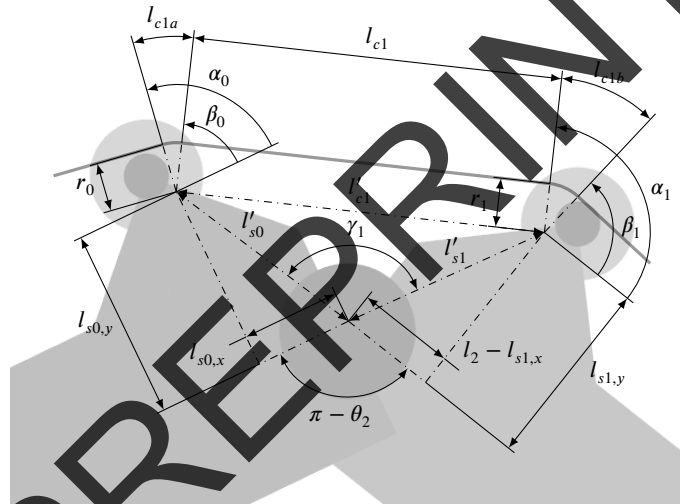
Figure 20: The geometry required to calculate the cable length across the knuckle joint.

$$\alpha_1 = \pi - \cos^{-1}\left(\frac{(l'_{s1})^2 + (l'_{c1})^2 - (l'_{s0})^2}{2l'_{s1}l'_{c1}}\right) - \tan^{-1}\left(\frac{l_2 - l_{s1,x}}{l_{s1,y}}\right) - \tan^{-1}\left(\frac{r_0 - r_1}{l'_{c1}}\right), \tag{153}$$

and the lengths of cable wrapped around the sheaves l_{c1a} and l_{c1b} are

$$l_{c1a} = r_0(\alpha_0 - \beta_0), \tag{154}$$
$$l_{c1b} = r_1(\alpha_1 - \beta_1). \tag{155}$$

Using the geometry shown in Figure 21, the length of the cable l_{c2} spanning the jib can be found by first calculating the intermediate length l'_{c2},

$$l'_{c2} = \sqrt{(l_{s1,x} + d_3)^2 + (l_{s1,y} - l_{4,y})^2}, \tag{156}$$

$$l_{c2} = \sqrt{(l'_{c2})^2 - (r_1 - r_2)^2}, \tag{157}$$

Figure 21: The geometry required to calculate the cable length along the jib

and the cable exit angle β_1 is given by

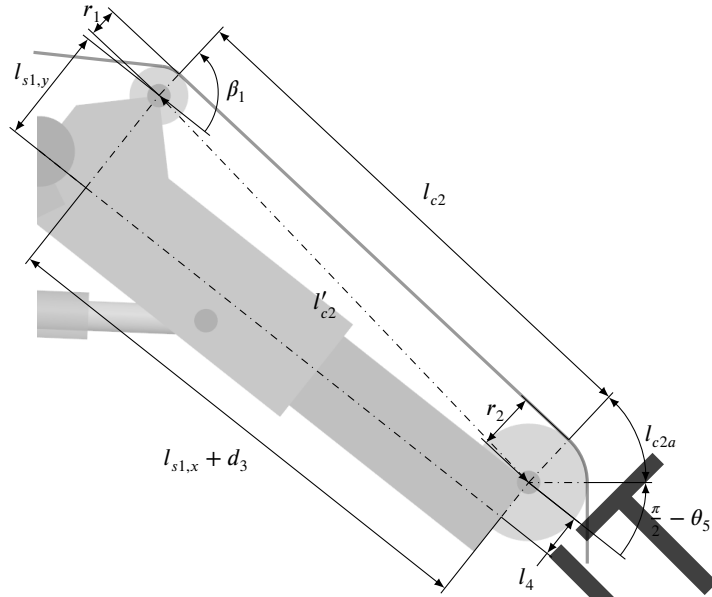$$\beta_1 = \cos^{-1}\left(\frac{r_1 - r_2}{l'_{c2}}\right) - \tan^{-1}\left(\frac{l_{s1,y} - l_{4,y}}{l_{s1,x} + d_3}\right). \tag{158}$$

The length of cable l_{c2a} wrapped around the tip sheave is given by

$$l_{c2a} = r_2\left(\beta_1 - \frac{\pi}{2} + \theta_5\right). \tag{159}$$

Therefore, the total length of cable l_c running along the crane from the tip of the sheave back to the winch is given by

$$l_c = l_{c0} + l_{c1} + l_{c1a} + l_{c1b} + l_{c2} + l_{c2a}, \tag{160}$$

which is a function of two degrees of freedom, the jib angle θ_2, which in turn is a function of the acutator extension d_2, and the jib extension length d_3.

D. Position Kinematics with Dual Quaternions

Using the coordinate frames in Figures 4, 5 and 6, along with the DH parameters presented in Tables 1, 2 and 3 for the main kinematic chain, boom actuator kinematic chain and jib actuator kinematic chain, respectively, dual quaternions representing the transformations between each coordinate frame can be built using equations (24)-(28). For the main kinematic chain, the dual quaternions are

$$^DQ_1 = \frac{\sqrt{2}}{2}\cos\left(\frac{\theta_0}{2}\right) + \left\{\begin{array}{c} -\frac{\sqrt{2}}{2}\cos\left(\frac{\theta_0}{2}\right) \\ -\frac{\sqrt{2}}{2}\sin\left(\frac{\theta_0}{2}\right) \\ \frac{\sqrt{2}}{2}\sin\left(\frac{\theta_0}{2}\right) \end{array}\right\}^T + \epsilon\left(-\frac{\sqrt{2}}{2}\sin\left(l_0\frac{\theta_0}{2}\right) + \left\{\begin{array}{c} l_0\frac{\sqrt{2}}{2}\sin\left(\frac{\theta_0}{2}\right) \\ -l_0\frac{\sqrt{2}}{2}\cos\left(\frac{\theta_0}{2}\right) \\ l_0\frac{\sqrt{2}}{2}\cos\left(\frac{\theta_0}{2}\right) \end{array}\right\}^T\right), \tag{161}$$

$$
{}^{1}Q_2 = \cos\left(\frac{\theta_1}{2}\right) + \left\{\begin{array}{c} 0 \\ 0 \\ \sin\left(\frac{\theta_1}{2}\right) \end{array}\right\}^{T} + \epsilon\left(0 + \left\{\begin{array}{c} l_1 \cos\left(\frac{\theta_1}{2}\right) \\ l_1 \sin\left(\frac{\theta_1}{2}\right) \\ 0 \end{array}\right\}^{T}\right), \tag{162}
$$

$$
{}^{2}Q_3 = \cos\left(\frac{\theta_2}{2}\right) + \left\{\begin{array}{c} 0 \\ 0 \\ \sin\left(\frac{\theta_2}{2}\right) \end{array}\right\}^{T} + \epsilon\left(0 + \left\{\begin{array}{c} l_2 \cos\left(\frac{\theta_2}{2}\right) \\ l_2 \sin\left(\frac{\theta_2}{2}\right) \\ 0 \end{array}\right\}^{T}\right), \tag{163}
$$

$$
{}^{3}Q_4 = 1 + \left\{\begin{array}{c} 0 \\ 0 \\ 0 \end{array}\right\}^{T} + \epsilon\left(0 + \left\{\begin{array}{c} d_3 \\ 0 \\ 0 \end{array}\right\}^{T}\right), \tag{164}
$$

$$
{}^{4}Q_5 = \frac{\sqrt{2}}{2} + \left\{\begin{array}{c} 0 \\ 0 \\ -\frac{\sqrt{2}}{2} \end{array}\right\}^{T} + \epsilon\left(0 + \left\{\begin{array}{c} l_4 \frac{\sqrt{2}}{2} \\ -l_4 \frac{\sqrt{2}}{2} \\ 0 \end{array}\right\}^{T}\right), \tag{165}
$$

$$
{}^{5}Q_6 = \cos\left(\frac{\theta_5}{2}\right) + \left\{\begin{array}{c} 0 \\ 0 \\ \sin\left(\frac{\theta_5}{2}\right) \end{array}\right\}^{T} + \epsilon\left(0 + \left\{\begin{array}{c} r_2 \cos\left(\frac{\theta_5}{2}\right) \\ r_2 \sin\left(\frac{\theta_5}{2}\right) \\ 0 \end{array}\right\}^{T}\right), \tag{166}
$$

$$
{}^{6}Q_7 = \frac{\sqrt{2}}{2}\cos\left(\frac{\theta_6}{2}\right) + \left\{\begin{array}{c} \frac{\sqrt{2}}{2}\cos\left(\frac{\theta_6}{2}\right) \\ \frac{\sqrt{2}}{2}\sin\left(\frac{\theta_6}{2}\right) \\ \frac{\sqrt{2}}{2}\sin\left(\frac{\theta_6}{2}\right) \end{array}\right\}^{T} + \epsilon\left(0 + \left\{\begin{array}{c} 0 \\ 0 \\ 0 \end{array}\right\}^{T}\right), \tag{167}
$$

$$
{}^{7}Q_8 = \cos\left(\frac{\theta_7}{2}\right) + \left\{\begin{array}{c} 0 \\ 0 \\ \sin\left(\frac{\theta_7}{2}\right) \end{array}\right\}^{T} + \epsilon\left(0 + \left\{\begin{array}{c} 0 \\ 0 \\ 0 \end{array}\right\}^{T}\right), \tag{168}
$$

$$
{}^{8}Q_9 = 1 + \left\{\begin{array}{c} 0 \\ 0 \\ 0 \end{array}\right\}^{T} + \epsilon\left(0 + \left\{\begin{array}{c} l_8 \\ 0 \\ 0 \end{array}\right\}^{T}\right). \tag{169}
$$

For the boom actuator kinematic chain, the dual quaternions are

$$
{}^{D}Q_{b1} = \frac{\sqrt{2}}{2}\cos\left(\frac{\theta_0}{2}\right) + \left\{\begin{array}{c} -\frac{\sqrt{2}}{2}\cos\left(\frac{\theta_0}{2}\right) \\ -\frac{\sqrt{2}}{2}\sin\left(\frac{\theta_0}{2}\right) \\ \frac{\sqrt{2}}{2}\sin\left(\frac{\theta_0}{2}\right) \end{array}\right\}^{T} + \epsilon\left(0 + \left\{\begin{array}{c} 0 \\ 0 \\ 0 \end{array}\right\}^{T}\right), \tag{170}
$$

$$
{}^{b1}Q_{b2} = \cos\left(\frac{\theta_{b1}}{2}\right) + \left\{\begin{array}{c} 0 \\ 0 \\ \sin\left(\frac{\theta_{b1}}{2}\right) \end{array}\right\}^{T} + \epsilon\left(0 + \left\{\begin{array}{c} l_{b1}\cos\left(\frac{\theta_{b1}}{2}\right) \\ l_{b1}\sin\left(\frac{\theta_{b1}}{2}\right) \\ 0 \end{array}\right\}^{T}\right), \tag{171}
$$

$$^{b2}Q_{b3} = \cos\left(\frac{\theta_{b2}}{2}\right) + \left\{\begin{array}{c} 0 \\ 0 \\ \sin\left(\frac{\theta_{b2}}{2}\right) \end{array}\right\}^{T} + \epsilon\left(0 + \left\{\begin{array}{c} l_{b2}\cos\left(\frac{\theta_{b2}}{2}\right) \\ l_{b2}\sin\left(\frac{\theta_{b2}}{2}\right) \\ 0 \end{array}\right\}^{T}\right), \tag{172}$$

$$^{b3}Q_{b4} = 1 + \left\{\begin{array}{c} 0 \\ 0 \\ 0 \end{array}\right\}^{T} + \epsilon\left(0 + \left\{\begin{array}{c} d_1 \\ 0 \\ 0 \end{array}\right\}^{T}\right), \tag{173}$$

And for the jib actuator kinematic chain, the dual quaternions are

$$^{1}Q_{c1} = \cos\left(\frac{\theta_{c1}}{2}\right) + \left\{\begin{array}{c} 0 \\ 0 \\ \sin\left(\frac{\theta_{c1}}{2}\right) \end{array}\right\}^{T} + \epsilon\left(0 + \left\{\begin{array}{c} l_{c1}\cos\left(\frac{\theta_{c1}}{2}\right) \\ l_{c1}\sin\left(\frac{\theta_{c1}}{2}\right) \\ 0 \end{array}\right\}^{T}\right), \tag{174}$$

$$^{c1}Q_{c2} = \cos\left(\frac{\theta_{c2}}{2}\right) + \left\{\begin{array}{c} 0 \\ 0 \\ \sin\left(\frac{\theta_{c2}}{2}\right) \end{array}\right\}^{T} + \epsilon\left(0 + \left\{\begin{array}{c} l_{c2}\cos\left(\frac{\theta_{c2}}{2}\right) \\ l_{c2}\sin\left(\frac{\theta_{c2}}{2}\right) \\ 0 \end{array}\right\}^{T}\right), \tag{175}$$

$$^{c2}Q_{c3} = 1 + \left\{\begin{array}{c} 0 \\ 0 \\ 0 \end{array}\right\}^{T} + \epsilon\left(0 + \left\{\begin{array}{c} d_2 \\ 0 \\ 0 \end{array}\right\}^{T}\right), \tag{176}$$

Dual quaternions can also be defined relating the centres of mass of each rigid body to one of the coordinate frames,

$$^{1}Q_{cog0} = 1 + \begin{bmatrix} 0 & 0 & 0 \end{bmatrix} + \epsilon\left(0 + \begin{bmatrix} -l_{cog0,x} & l_{cog0,y} & 0 \end{bmatrix}\right), \tag{177}$$

$$^{2}Q_{cog1} = 1 + \begin{bmatrix} 0 & 0 & 0 \end{bmatrix} + \epsilon\left(0 + \begin{bmatrix} -l_{cog1,x} & -l_{cog1,y} & 0 \end{bmatrix}\right), \tag{178}$$

$$^{3}Q_{cog2} = 1 + \begin{bmatrix} 0 & 0 & 0 \end{bmatrix} + \epsilon\left(0 + \begin{bmatrix} -l_{cog2,x} & -l_{cog2,y} & 0 \end{bmatrix}\right), \tag{179}$$

$$^{4}Q_{cog3} = 1 + \begin{bmatrix} 0 & 0 & 0 \end{bmatrix} + \epsilon\left(0 + \begin{bmatrix} -l_{cog3,x} & -l_{cog3,y} & 0 \end{bmatrix}\right), \tag{180}$$

$$^{2}Q_{w} = 1 + \begin{bmatrix} 0 & 0 & 0 \end{bmatrix} + \epsilon\left(0 + \begin{bmatrix} -l_{w,x} & -l_{w,y} & 0 \end{bmatrix}\right), \tag{181}$$

$$^{2}Q_{s0} = 1 + \begin{bmatrix} 0 & 0 & 0 \end{bmatrix} + \epsilon\left(0 + \begin{bmatrix} -l_{s0,x} & -l_{s0,y} & 0 \end{bmatrix}\right), \tag{182}$$

$$^{3}Q_{s1} = 1 + \begin{bmatrix} 0 & 0 & 0 \end{bmatrix} + \epsilon\left(0 + \begin{bmatrix} -l_{s1,x} & -l_{s1,y} & 0 \end{bmatrix}\right), \tag{183}$$

$$^{b3}Q_{cogb1} = 1 + \begin{bmatrix} 0 & 0 & 0 \end{bmatrix} + \epsilon\left(0 + \begin{bmatrix} -l_{cogb1} & 0 & 0 \end{bmatrix}\right), \tag{184}$$

$$^{b4}Q_{cogb2} = 1 + \begin{bmatrix} 0 & 0 & 0 \end{bmatrix} + \epsilon\left(0 + \begin{bmatrix} -l_{cogb2} & 0 & 0 \end{bmatrix}\right), \tag{185}$$

$$^{c2}Q_{cogc1} = 1 + \begin{bmatrix} 0 & 0 & 0 \end{bmatrix} + \epsilon\left(0 + \begin{bmatrix} -l_{cogc1} & 0 & 0 \end{bmatrix}\right), \tag{186}$$

$$^{c3}Q_{cogc2} = 1 + \begin{bmatrix} 0 & 0 & 0 \end{bmatrix} + \epsilon\left(0 + \begin{bmatrix} -l_{cogc2} & 0 & 0 \end{bmatrix}\right), \tag{187}$$

Concatenating the dual quaternions provides a dual quaternion relating the transformation of each centre of gravity with respect to the deck coordinate frame,

$$^{D}Q_{cog0} = {}^{D}Q_1 {}^{1}Q_{cog0}, \tag{188}$$

$$^{D}Q_{cog1} = {}^{D}Q_1 {}^{1}Q_2 {}^{2}Q_{cog1}, \tag{189}$$

$$^{D}Q_{cog2} = {}^{D}Q_1 {}^{1}Q_2 {}^{2}Q_3 {}^{3}Q_{cog2}, \tag{190}$$

$$^{D}Q_{cog3} = {}^{D}Q_1 {}^{1}Q_2 {}^{2}Q_3 {}^{3}Q_{cog3}, \tag{191}$$

$$^{D}Q_{w} = {^{D}Q_1}{^{1}Q_2}{^{2}Q_w},$$ (192)

$$^{D}Q_{s0} = {^{D}Q_1}{^{1}Q_2}{^{2}Q_{s0}},$$ (193)

$$^{D}Q_{s1} = {^{D}Q_1}{^{1}Q_2}{^{2}Q_3}{^{3}Q_{s1}},$$ (194)

$$^{D}Q_{s2} = {^{D}Q_1}{^{1}Q_2}{^{2}Q_3}{^{3}Q_4}{^{4}Q_5},$$ (195)

$$^{D}Q_{pay} = {^{D}Q_1}{^{1}Q_2}{^{2}Q_3}{^{3}Q_4}{^{4}Q_5}{^{5}Q_6}{^{6}Q_7}{^{7}Q_8}{^{8}Q_9},$$ (196)

$$^{D}Q_{cogb1} = {^{D}Q_{b1}}{^{b1}Q_{b2}}{^{b2}Q_{b3}}{^{b3}Q_{cogb1}},$$ (197)

$$^{D}Q_{cogb2} = {^{D}Q_{b1}}{^{b1}Q_{b2}}{^{b2}Q_{b3}}{^{b3}Q_{b4}}{^{b4}Q_{cogb2}},$$ (198)

$$^{D}Q_{cogc1} = {^{D}Q_1}{^{1}Q_{c1}}{^{c1}Q_{c2}}{^{c2}Q_{cogc1}},$$ (199)

$$^{D}Q_{cogc1} = {^{D}Q_1}{^{1}Q_{c1}}{^{c1}Q_{c2}}{^{c2}Q_{c3}}{^{c3}Q_{cogc2}}.$$ (200)

Note that as with transformation matrices, a dual quaternion product is non-commutative, and each expression must be evaluated from left to right.

The rotation matrices between the deck coordinate frame and centre of mass i area also required to rotate the inertia matrices into the deck coordinate frame. Given a dual quaternion $^{D}Q_i = (q_0, q_1, q_2, q_3, p_0, p_1, p_2, p_3)$, the corresponding rotation matrix $^{D}R_i$ is

$$^{D}R_i = \begin{bmatrix} q_0^2 + q_1^2 - q_2^2 - q_3^2 & 2(q_1q_2 - q_0q_3) & 2(q_0q_2 + q_1q_3) \\ 2(q_1q_2 + q_0q_3) & q_0^2 - q_1^2 + q_2^2 - q_3^2 & 2(q_2q_3 - q_0q_1) \\ 2(q_1q_3 - q_0q_2) & 2(q_0q_1 + q_2q_3) & q_0^2 - q_1^2 - q_2^2 + q_3^2 \end{bmatrix}.$$ (201)

E. Simulation Properties and Gains

The geometric and inertial properties of the knuckle boom crane are provided in Table 7, and the gains for the sliding mode controller are presented in Table 8. For the nonlinear trajectory optimizer, $\kappa = 1$, $i_{max} = 5$, and $\delta_{1,max} = \delta_{2,max} = \delta_{3,max} = \delta_{4,max} = 0.001$. For the trajectory modifier, $\epsilon_x = \epsilon_y = 0.0001$, $\epsilon_z = \epsilon_l = 0.01$, $\xi_{x,min} = \xi_{x,min} = 0.5$, $\xi_{x,max} = \xi_{y,max} = 1.5$, $\xi_{z,min} = \xi_{l,min} = -1$ and $\xi_{z,max} = \xi_{l,max} = 1$. For the actuator transfer functions, $b_1 = b_2 = b_3 = b_4 = b_5 = 10$.

Table 7
Knuckle Boom Crane Model Parameters

Geometric		Inertial	
Parameter	Value	Parameter	Value
l_0	4 m	m_0	5000 kg
l_1	4 m	m_1	3000 kg
l_2	3 m	m_2	2000 kg
$l_{b1,x}$	0.8 m	m_3	1500 kg
$l_{b1,z}$	1 m	m_w	500 kg
$l_{b4,x}$	1 m	$m_{s0} = m_{s1}$	250 kg
$l_{b4,y}$	0.5 m	m_{s2}	500 kg
$l_{c1,x}$	2 m	m_p	1770 kg
$l_{c1,y}$	0.5 m	$m_{b1} = m_{c1}$	1000 kg
$l_{c3,x}$	2 m	$m_{b2} = m_{c2}$	1000 kg
$l_{c3,y}$	0.5 m	$I_{xx,0}$	7083.33 kgm^2
l_{b2}	2 m	$I_{yy,0}$	833.33 kgm^2
l_{c2}	2 m	$I_{zz,0}$	7083.33 kgm^2
$l_{cog0,x}$	0 m	$I_{xx,1}$	390.63 kgm^2
$l_{cog0,y}$	2 m	$I_{yy,1}$	4140.63 kgm^2
$l_{cog1,x}$	2 m	$I_{zz,1}$	4250.00 kgm^2
$l_{cog1,y}$	0 m	$I_{xx,2}$	208.33 kgm^2
$l_{cog2,x}$	1.5 m	$I_{yy,2}$	1541.67 kgm^2
$l_{cog2,y}$	0 m	$I_{zz,2}$	1666.67 kgm^2
$l_{cog3,x}$	1 m	$I_{xx,3}$	90.31 kgm^2
$l_{cog3,y}$	0 m	$I_{yy,3}$	520.00 kgm^2
$l_{cog,b1}$	1 m	$I_{zz,3}$	570.31 kgm^2
$l_{cog,b2}$	1.25 m	$I_{xx,w} = I_{xx,s2}$	33.85 kgm^2
$l_{cog,c1}$	1 m	$I_{yy,w} = I_{yy,s2}$	33.85 kgm^2
$l_{cog,c2}$	1.25 m	$I_{zz,w} = I_{zz,s2}$	62.50 kgm^2
$l_{w,x}$	3.5 m	$I_{xx,s0} = I_{xx,s1}$	5.21 kgm^2
$l_{w,y}$	1 m	$I_{yy,s0} = I_{yy,s1}$	5.21 kgm^2
$l_{s0,x}$	0.5 m	$I_{zz,s0} = I_{zz,s1}$	7.81 kgm^2
$l_{s0,y}$	1 m	J_a	3.125 kgm^2
$l_{s1,x}$	2.5 m	$I_{xx,b1} = I_{xx,c1}$	40 kgm^2
$l_{s1,y}$	1 m	$I_{yy,b1} = I_{yy,c1}$	900 kgm^2
l_4	0.375 m	$I_{zz,b1} = I_{zz,c1}$	900 kgm^2
r_w	0.5 m	$I_{xx,b2} = I_{xx,c2}$	10 kgm^2
r_0	0.25 m	$I_{yy,b1} = I_{yy,c1}$	650 kgm^2
r_1	0.25 m	$I_{zz,b1} = I_{zz,c1}$	650 kgm^2
r_2	0.5 m	N	4

Table 8
Knuckle Boom Crane SMC Controller Gains

λ_1	20	$k_{\alpha,1}$	5E5	$\Phi_{\alpha,1}$	10	$k_{\beta,1}$	1E5	$\Phi_{\beta,1}$	1E4
λ_2	20	$k_{\alpha,2}$	5E5	$\Phi_{\alpha,2}$	10	$k_{\beta,2}$	1E5	$\Phi_{\beta,2}$	1E4
λ_3	20	$k_{\alpha,3}$	5E5	$\Phi_{\alpha,3}$	10	$k_{\beta,3}$	5E4	$\Phi_{\beta,3}$	1E4
λ_4	20	$k_{\alpha,4}$	1E5	$\Phi_{\alpha,4}$	10	$k_{\beta,4}$	1E4	$\Phi_{\beta,4}$	1E4
λ_5	20	$k_{\alpha,5}$	1E4	$\Phi_{\alpha,5}$	1	$k_{\beta,5}$	1E4	$\Phi_{\beta,5}$	1E4
λ_6	20	$k_{\alpha,6}$	0	$\Phi_{\alpha,6}$	0	$k_{\beta,6}$	0	$\Phi_{\beta,6}$	0
λ_7	20	$k_{\alpha,6}$	0	$\Phi_{\alpha,6}$	0	$k_{\beta,6}$	0	$\Phi_{\beta,6}$	0

CRediT authorship contribution statement

Iain A. Martin: Methodology, Software, Validation, Formal analysis, Writing - Original Draft, Visualization. **Rishad A. Irani:** Conceptualization, Resources, Investigation, Data Curation, Writing - Review & Editing, Supervision, Project administration, Funding acquisition.

References

[1] Adamiec-Wójcik, I., et al., 2019. A 3d model for static and dynamic analysis of an offshore knuckle boom crane. Applied Mathematical Modelling 66, 256–274.

[2] Bak, M., Hansen, M., 2013a. Analysis of offshore knuckle boom crane - part one: Modeling and parameter identification. Modeling, Identification and Control 34(4), 157–174.

[3] Bak, M., Hansen, M., 2013b. Analysis of offshore knuckle boom crane - part two: Motion control. Modeling, Identification and Control 34(4), 175–181.

[4] Bertsekas, D., 1999. Nonlinear Programming, Second Edition. Athena Scientific.

[5] Cao, Y., Li, T., 2020. Review of antiswing control of shipboard cranes. IEEE/CAA Journal of Automatica Sinica 7(2), 346–354.

[6] Cibicik, A., Egeland, O., 2019. Dynamic modelling and force analysis of a knuckle boom crane using screw theory. Mechanism and Machine Theory 133, 179–194.

[7] Cibicik, A., Pedersen, E., Egeland, O., 2020. Dynamics of luffing motion of a flexible knuckle boom crane actuated by hydraulic cylinders. Mechanism and Machine Theory 143, 103616.

[8] Cibicik, A., Tysse, G., Egeland, O., 2019. Determination of reaction force of a deck crane in wave motion using screw theory. Journal of Offshore Mechanics and Arctic Engineering 141, 061604.

[9] Clifford, W.K., 1873. Preliminary sketch of bi-quaternions. Proceedings of the London Mathematical Society 4(1), 286–298.

[10] Funda, J., Taylor, R.H., Paul, R.P., 2018. On homogeneous transforms, quaternions and computational efficiency. International Journal of Control, Automation and Systems 16(2), 559–565.

[11] Hamilton, W.R., 1844 - 1850. On quaternions, or on a new system of imaginaries in algebra. London, Edinburgh, and Dublin Philosophical Magazine and Journal of Science .

[12] Heila, 2020. Foldable Telescopic Cranes. Heila Cranes.

[13] Hiab, 2020. Hiab Sea Crane Brochure. Hiab.

[14] Kim, D., Park, Y., 1999. Tracking control in x-y plane of an offshore container crane. Trans. of the Society of Instrument and Control Engineers 35(2), 253–261.

[15] Kim, G., 2020. Continuous integral sliding mode control of an offshore container crane with input saturation. International Journal of Control, Automation and Systems 18, 1–11.

[16] Kim, G., Hong, K., 2019. Adaptive sliding mode control of an offshore container crane with unknown disturbances. IEEE/ASME Transactions on Mechatronics .

[17] Maghsoudi, M., et al., 2019. Improved unity magnitude input shaping scheme for sway control of an underactuated 3d overhead crane with hoisting. Mechanical Systems and Signal Processing 123, 466–482.

[18] Martin, I., Irani, R., 2019. Evaluation of both linear and non-linear control strategies for a shipboard marine gantry crane, in: Oceans Seattle 2019.

[19] Martin, I., Irani, R., 2020. A generalized approach to anti-sway control for shipboard cranes. Submitted to Mechanical Systems and Signal Processing .

[20] McTaggart, K., 2011. ShipMo3D version 3.0 user manual for computing ship motions in the time and frequency domains. Defense Research and Development Canada - Atlantic (DRDC - Atlantic). Dartmouth, Nova Scotia. TM 2011-308.

[21] McTaggart, K., 2012. Validation of ShipMo3D version 3.0 user applications for simulation ship motions. Defense Research and Development Canada - Atlantic (DRDC - Atlantic). Dartmouth, Nova Scotia. TM 2011-306.

[22] Palfinger, 2020. Palfinger Marine Product Brochure. Palfinger Marine GmbH.

[23] Ramli, L., Mohamed, Z., Jaafar, H., 2018. A neural network-based input shaping for swing suppression of an overhead crane under payload hoisting and mass variations. Mechanical Systems and Signal Processing 107, 484–501.

[24] Ramli, L., et al., 2017. Control strategies for crane systems: A comprehensive review. Mechanical Systems and Signal Processing 95, 1–23.

[25] Ramli, L., et al., 2020. Efficient swing control of an overhead crane with simultaneous payload hoisting and external disturbances. Mechanical Systems and Signal Processing 135, 106326.

[26] Tysse, G., Egeland, O., 2018. Dynamic interaction of a heavy crane and a ship in wave motion. Modeling, Identification and Control 39(2), 45–60.

[27] Tysse, G., Egeland, O., 2019. Crane load position control using lyapunov-based pendulum damping and nonlinear mpc position control, in: Proceedings of The 18th European Control Conference (ECC).

[28] Wang, S., et al., 2018. Dynamic modelling and analysis of 3-axis motion compensated offshore cranes. Ships and Offshore Structures 13(3), 265–272.